MEASURING THE INSTRUMENT FUNCTION OF RADIOMETERS

Roland Winston
Enrico Fermi Institute
The University of Chicago
Chicago, Illinois 60637, U.S.A.

Robert G. Littlejohn
Department of Physics, University of California
Berkeley, Ca 94720, U.S.A.

ABSTRACT

The instrument function is a function of position and angle, the knowledge of which allows one to compute the response of a radiometer to an incident wave field in any state of coherence. The instrument function of a given radiometer need not be calculated; instead, it may be measured by calibration with incident plane waves.

INTRODUCTION

Since the pioneering work of Walther [1], it has been widely understood that the state of an optical field, including its coherence properties, can be described by a single function (the generalized radiance) which depends on position (x) and angle (or, equivalently, transverse wave number k). The generalized radiance contains all the information available in the various second order correlation functions. The subject of radiometry and coherence has been developed and reviewed by Wolf and coworkers [2]. However, the generalized radiance presents some conceptual difficulties because it can take on negative values in certain regions of the (x,k) phase space, in spite of the fact that the results of all physical radiometric measurements are nonnegative.

In a recent paper [3], we showed how the result of a physical measurement can be represented as the phase-space overlap or scalar product of the generalized radiance with a function which characterizes the instrument. We call the latter function the "instrument function"; like the generalized radiance, it is a function of (x , k). Explicitly, we have

$$Q = 1/2\pi \int dx\, dk\, W(x,k)\, M(x,k) \qquad (1)$$

where Q is the result of the measurement, W (x ,k) is the generalized radiance (according to Walther [1]) and M(x ,k) is the instrument function. Our use of the instrument function is similar to an approach taken earlier by Gase, Ponath and Schubert [4]. As in Ref.3, we keep to a one-dimensional model to bring out the physical ideas without complicating the mathematics.

Thus, the result of a physical measurement is expressed in terms of two functions, one of which (W) characterizes the radiation field, and the other of which (M) characterizes the instrument. Furthermore, the mathematical theory of the Wigner function [5] makes it manifest that the physical result is nonnegative-definite.

In the same paper [3] we calculated the instrument function for a simple radiometer. However, the calculation does not apply universally to all radiometers; in particular not to nonimaging concentrators whose uniform phase-space acceptance properties are attractive for radiometric measurements [6]. Rather than leave the impression that each radiometer design requires a potentially tedious calculation, we show in this paper how the instrument may be calibrated. Calibration is, after all, the common practice and preferred means of using radiometers in the first place.

In this paper we will not discuss any specific radiometer design, since it is our purpose to treat the radiometer as a black box, which merely transforms the incident wave field into a nonnegative definite output signal. Nor is there any assumption that geometrical optics is valid in the inner workings of the instrument; the effects of diffraction, interference, and partial coherence are fully incorporated. All of this is made evident by the theory of the instrument function which was presented in Ref. 3.

SINGLE PLANE WAVE METHOD

Calibration with a single plane wave does not suffice to measure the instrument function of a radiometer for all values of (x , k), because the generalized radiance of a plane wave is uniform over the aperture of the radiometer. However, the information so obtained is sufficient to determine the response of the radiometer in all other circumstances in which the generalized radiance is essentially uniform across the radiometer, including many cases of incoherent, distant sources. We note that whenever the 2-point correlation function of the field, Γ (x,x') , factors into a slow function of x+x' times a rapid function of x-x' , the generalized radiance will itself be a slow

function of x, perhaps sufficiently slow to be sensibly constant over the aperture of the instrument. The condition in question is the same as that which appears in Carter's and Wolf's [7] definition of "quasihomogeneity", except that as far as we can see those authors are thinking of the state of the radiation field at a source, whereas we are referring to the state of the field at the entrance aperture of the instrument.

Varying the incident direction sweeps out the beam-pattern response of the instrument. Let the plane wave in the x,z plane be $\Psi(x,z) = A \exp[i(k_t x + k_l z)]$, where k_t and k_l are respectively the transverse and longitudinal wave numbers. The generalized radiance W is determined from the transverse part of the wave field $\psi(x)$ according to

$$W(x,k) = \int ds\, e^{-iks} \langle \psi(x+s/2)\, \psi^*(x-s/2) \rangle, \tag{2}$$

where the angle brackets represent the statistical average. In the present case,

$$\psi(x) = A \exp(i k_t x)\ , \text{ so}$$

$$W(x,k) = 2\pi |A|^2 \delta(k-k_t). \tag{3}$$

The statistical average is unnecessary in this case because the light is coherent.

Then according to Eq. (1), the result of the measurement is

$$Q = |A|^2 \int dx\, M(x,k_t), \tag{4}$$

where 2 a is the aperture of the radiometer. This shows that the spatial integral of the instrument function M can be determined by calibrating with a single plane wave.

DOUBLE PLANE WAVE METHOD

There are important circumstances in which the generalized radiance is not constant over the aperture of the instrument. For example, often coherent wave fields will generate interference patterns on a scale comparable to or smaller than the aperture. For another example, consider an edge back-

illuminated by an incoherent source, or, equivalently, an incoherent source with a sharp edge. In this case, the best compromise between spatial and angular resolution is obtained by setting $a \approx \sqrt{\lambda z}$ and $\theta \approx \sqrt{\lambda/z}$, i.e., making the size of the aperture comparable to the blurring of the edge from Fresnel diffraction, and making the instrument accept a single cell in phase space. Yet another counter-example is any nearby source. For such applications, we need more detailed information concerning the instrument function.

Therefore we now consider calibrating with a pair of mutually coherent plane waves, which produce the transverse wave field

$$\psi(x) = A\exp(ik_1 x) + A\exp(ik_2 x) , \tag{5}$$

where k_1 and k_2 are the transverse wave numbers. Such a pair of plane waves might, for example, be prepared by a single plane wave incident on a beam-splitter. Then according to Eq. (2) we find

$$W(x,k) = 2\pi \{ |A_1|^2 \delta(k - k_1) + A_2|^2 \delta(k - k_2) + \tag{6}$$
$$[A_1 A_2^* \exp i(k_1 - k_2) + c.c.] \delta[k - (k_1 + k_2)/2] \}$$

The first two terms are the generalized radiance functions of the two incident plane waves taken one at a time, while the third term contains the interference effects. By subtracting the results of two single plane wave calibrations as described above, we can measure the quantity

$$Q_{reduced} = \int dx \, M(x,k_+)[A_1 A_2^* \exp i(k_- x) + c.c.] \tag{7}$$

where

$$k_+ = (k_1 + k_2)/2 , \quad k_- = (k_1 - k_2) \tag{8}$$

First consider the case that A_1 and A_2 are in phase, say, $A_1 = |A_1| \exp i\alpha$ and $A_2 = |A_2| \exp i\alpha$. Then by holding k_+ fixed and varying k_-, we obtain

$$Q_c = 2|A_1||A_2| \int dx \, M(x,k_+) \cos(k_- x) , \tag{9}$$

which is the cosine transform of M in x for a fixed value of k. On the other hand, if A_1 and A_2 are $\pi/2$ out of phase, say, $A_1 = |A_1| \exp i\alpha$ and $A_2 = |A_2| \exp i\alpha+i\pi/2$, then we obtain

$$Q_s = 2|A_1||A_2| \int dx \ M(x,k_+) \sin(k_- x) \tag{10}$$

which is the sine transform. Then the quantity $Q_c + i Q_s$ is proportional to the Fourier transform of M in x , which may be inverted to find M itself as a function of x and k. As was discussed in Ref. 3, the instrument function is appreciable in the acceptance region of the radiometer in phase space, as determined by geometrical optics; but it also has nonzero values outside this region, due to diffraction effects. On the other hand, M does fall off as one moves away from the geometrical acceptance region so the range of k values which must be examined in the calibration we propose is limited.

CONCLUSIONS

In classical radiometry, the instrument is routinely calibrated by measuring the beam-pattern angular acceptance of a distant (plane-wave) source. In the context of generalized raidometry we find that a complete specification requires measurement of a two-point angular correlation. Two-point angular correlation measurements are important in astrophysics in, for example, measurement of inhomogeneities in the cosmic three degree background radiation. It would be interesting to consider whether the interpretation of such measurements would require the kind of detailed information suggested in this paper.

ACKNOWLEDGMENT

REFERENCES

1. A. WALTHER, "Radiometry and Coherence," J. Opt. Soc. Am. 58, 1256-1259 (1968).

2. EMIL WOLF, "Coherence and Radiometry," J. Opt. Soc. Am. 68, 6-17 (1978).

3. ROBERT G. LITTLEJOHN and ROLAND WINSTON, "Generalized Radiance and Measurement," J. Opt. Soc. Am. A 12, 2736-2743 (1995).

4. R. GASE, H.-E. PONATH and M. SCHUBERT, "On a Temporal-Spatial Functional and its Measurement," Annalen der Physik 7, 487-498 (1986).

5. E. WIGNER, "On the Quantum Corrections for Thermodynamic Equilibrium," Phys. Rev. 40, 749-759 (1932).

6. W. T. WELFORD and R. WINSTON, High Collection Nonimaging Optics (Academic Press, New York and London, 1989).

7. W. H. CARTER and E. WOLF, "Coherence and Radiometry with Quasihomogeneous Planar Sources," J. Opt. Soc. Am. 67, 785-796 (1977).

Applications of Nonimaging Optics
for Very High Solar Concentrations

J. O'Gallagher and R. Winston
Enrico Fermi Institute
The University of Chicago

Abstract

Using the principles and techniques of nonimaging optics, solar concentrations that approach the theoretical maximum can be achieved. This has applications in solar energy collection wherever concentration is desired. In this paper, we survey recent progress in attaining and using high and ultrahigh solar fluxes. We review a number of potential applications for highly concentrated solar energy and the current status of the associated technology. By making possible new and unique applications for intense solar flux, these techniques have opened a whole new frontier for research and development of potentially economic uses of solar energy .

INTRODUCTION

In 1991, the solar energy research group at the University of Chicago measured solar flux levels exceeding those at the surface of the sun itself [1]. This remarkable achievement brought solar concentrator research into a new domain and served as a dramatic demonstration of the power of the techniques of nonimaging optics which allows the design of optical devices that approach the thermodynamic (ideal) limit, that is, the maximum possible concentration achievable for a given angular field of view. There are a whole family of single element nonimaging concentrators designed for relatively large acceptance angles, most notably the so called Compound Parabolic Concentrator or CPC. These are useful for achieving effective collection and concentration of sunlight at moderate to intermediate levels without tracking. The principles and applications of these designs are now well known and will not be discussed here. However for small angular acceptances and corresponding large concentration ratios, these single stage devices become extremely long and narrow and as such are not practical for attaining very high concentration, so that two-stage systems must be employed. In this report, we survey recent applications of a variety of two-stage designs using nonimaging secondaries which make possible the generation of high and ultra high solar fluxes .

THE THERMODYNAMIC LIMIT AND
THE CONCENTRATION SOLAR THERMAL ENERGY

The limit to which a beam of light can be concentrated (or deconcentrated) is fundamentally connected to its angular divergence, θ_i, by the well known **sine law of concentration** [2]. This is

$$C_{max} = \frac{n^2}{\sin^2(\theta_i)} \tag{1}$$

where n is the index of refraction at the target surface. Here θ_i is the total angular subtense of the source including all optical and pointing errors. For the case $n = 1$ and $\theta_i = \theta_s = 4.7$ milliradians, the half angular subtense of the sun, Eqn. (1) yields the well known limit of 46,000 on the concentration of terrestrial sunlight . This allows for no optical or tracking errors.
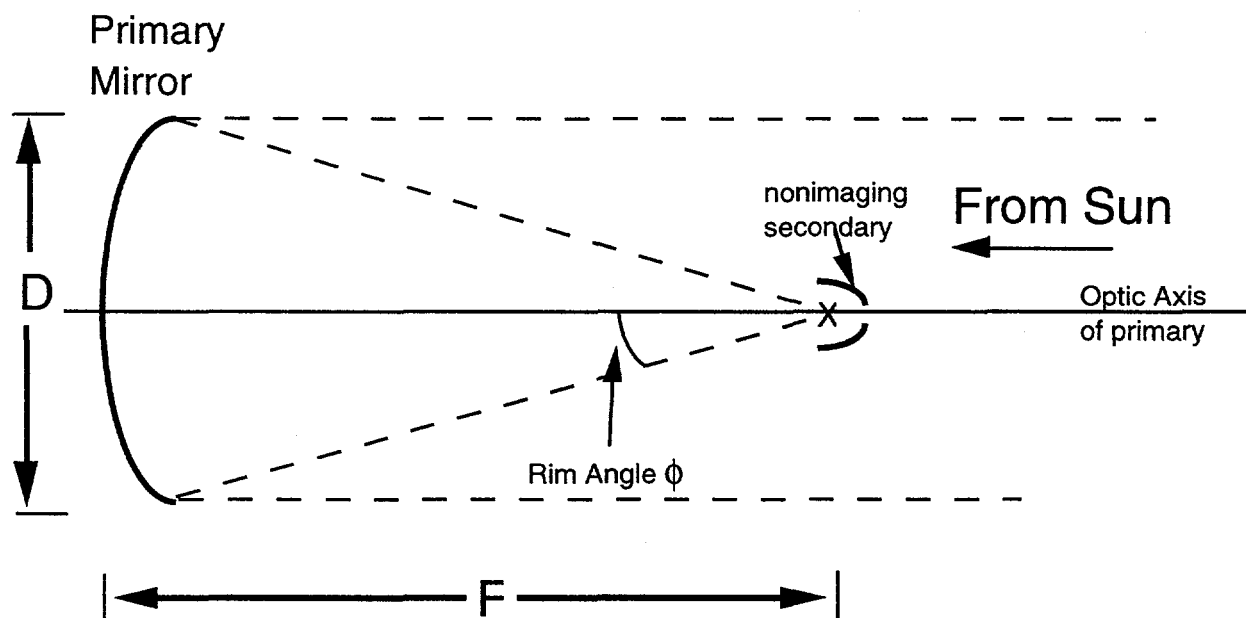
Primary Mirror

D

F

nonimaging secondary

From Sun

Optic Axis of primary

Rim Angle ϕ

Figure 1. Schematic summary of configuration for a two-stage nonimaging concentrator.

THE LIMITATIONS OF CONVENTIONAL FOCUSING CONCENTRATORS

An early impetus to the development of nonimaging optics was the realization that conventional imaging optics falls far short of the sine law limit. For example, a parabolic reflector achieves, at best, one quarter of the sine law limit. It is easily shown [2] that the concentration of a single stage paraboloid or any other conventional reflecting focussing primary falls well short of the limits of Equation 2. In particular, a primary with a convergence angle half-angle (or rim angle) ϕ, as schematically illustrated in Figure 2, can attain a geometrical concentration ratio of at most

$$C_{1, \max} = \frac{\cos^2\phi\sin^2\phi}{\sin^2(\theta_i)} \tag{2}$$

and thus falls short of the maximum limit by a factor of $\dfrac{n^2}{\cos^2\phi\sin^2\phi}$. The maximum value of Equation 2 occurs at $\phi = 45^\circ$, and thus, even for this best single stage concentrator, the shortfall with respect to the limit of Equation 1 is at least a factor of $4\,n^2$. However by a suitable choice of a secondary concentrator deployed in the focal zone of the primary or "first stage" one can recover much of this loss in concentration.

<u>Advantages and Features of Two-Stage Concentrating Systems</u> The most effective designs (currently in use) for attaining very high concentrations and approaching the thermodynamic limit with a practical system are the so-called two-stage configurations [3,4] comprised of a focusing first stage (or primary) and a nonimaging second stage (or secondary) deployed in the focal zone of the primary as indicated schematically in Figure 1. From Eqn. (1), we know that a nonimaging secondary can achieve a geometrical concentration factor of

$$C_{2,max} = \frac{n^2}{\sin^2\phi}$$
(3)

where ϕ is the rim angle of the primary. Combining this with the concentration of a single stage focusing primary (Eqn. 3) we find that the practical geometric limit (with a fixed acceptance secondary) is

$$C_{2\text{-stage, max}} = C_1 \bullet C_2 = \frac{n^2\cos^2\phi}{\sin^2\theta_i} \quad .$$
(4)

It should be recognized that the single stage limit of Equation 3 applies not only to paraboloids, but to *any concave focusing primary* (Welford and Winston, 1980). The two stage limit of Equation 5 comes close to the ideal limit of Equation (1) for small ϕ, i.e., for large focal length to diameter (F/D) ratios. The rim angle ϕ is related to the focal ratio $f = F/D$ by

$$\phi = \tan^{-1}[\frac{1}{(2f - 1/(8f))}]$$
(5)

Relative Concentration ratio

Comparative Concentration Limits

Focal Ratio (F/D)

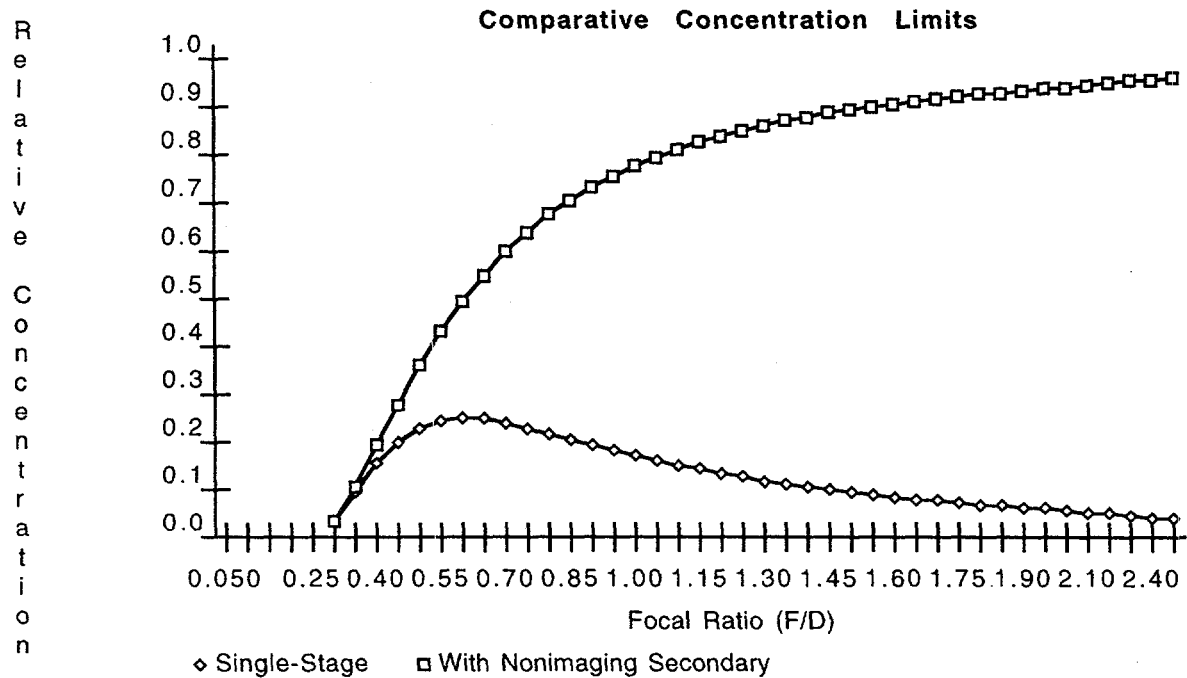◇ Single-Stage   ◻ With Nonimaging Secondary

Figure 2. Comparison of the maximum geometric concentration attainable by one and two stage systems with the ideal limit.

Design Considerations for Nonimaging Secondary Concentrators. There are three different regimes for applications. These are 1) ultra-high flux applications in air, 2) ultra-high flux applications in a refractive medium, and 3) conventional dish-thermal retrofit applications. Corresponding secondaries of choice in each of these regimes respectively are 1) Reflecting CPCs (or CECs) [3] , 2) Refracting Hi-Index Nonimaging concentrators; either dielectric filled CPCs (DCPCs) or Dielectric Totally Internally Reflecting Concentrators (DTIRCs) [5], and 3) flow-line or "trumpet" concentrators (Winston and Welford, 1979). Each of these types of secondaries has advantages and disadvantages and particular features that must be borne in mind in optimizing its design.

Demonstration and Measurement of Ultrahigh Solar Fluxes. Following through with a long-standing desire to explore the development of these techniques for larger scale, higher power applications, the National Renewable Energy Laboratory (NREL), formerly the Solar Energy Research Institute (SERI) designed and constructed a scaled-up solar concentrating furnace facility specifically intended to make use of nonimaging optics [6]. This High Flux Solar Furnace (HFSR) concept uses a modified long focal length design and is capable of delivering up to 10 Kilowatts to the focal zone and in particular to the entrance aperture of a secondary concentrator.

The measurement of ultrahigh fluxes may seem straightforward in principle, but it is difficult to implement in practice. For this reason, most of the high flux measurements based on these techniques rely on fluid based calorimetric measurements. Because of difficulties in measuring high fluxes in large scale high-index mediums, new techniques were developed [7,8,9] to extract light from higher index materials into a lower index ones. A new way to measure the flux passing through a large dielectric aperture developed from research at the Weizmann Institute of Science (WIS) in Israel and at the University of Chicago. These investigations studied the use of long extensions attached to the exit apertures of secondary nonimaging concentrators to extract light into air. A relatively simple device was developed that extracts light into air from a borosilicate medium (n=1.46) with an efficiency greater than 99%. New DTIRC secondaries were fabricated with such "extractor tips" . These secondaries were then combined with the cold water calorimeter developed for the air measurements and a successful measurement of the power delivered through a small aperture surrounding the "waist" of the extractor tip was carried out.

APPLICATIONS USING HIGHLY CONCENTRATED SUNLIGHT

Recent experiments and others performed at the National Renewable Energy Laboratory's (NREL) High Flux Solar Furnace (HFSF) have demonstrated the effectiveness of using concentrated sunlight and advanced nonimaging secondaries to pump lasers and produce fullerenes (potentially useful new forms of molecular carbon). The recently developed techniques that allow more flexibility in design [10] have been used to develop two new configurations, each of which couples the high solar flux available at the HFSF to unusually shaped targets which impose unusual constraints.

Solar-Pumped Lasers There are two methods for pumping lasers using sunlight, a) end-pumping and b) side-pumping. . There are advantages and disadvantages for each. The end-pumping scheme can be used on very small scales, but the pump light enters the laser crystal entirely from one end. Previous high-flux measurements show that this system can not be scaled up indefinitely as the optical coupling between dielectric surfaces degrades when exposed to ultrahigh solar fluxes at the kW power scale. An end-pumping scheme has a maximum output power to about 5 W. The side-pumping scheme doesn't face this limitation, because the lasing medium is excited sunlight entering over a much larger aperture (the side walls of the laser crystal). Current research suggests that space-based applications hold the most promise for solar

lasers. In space, the solar insolation level, the input pump source, is more intense and much more stable. This in turn allows more stable lasing configurations that increase laser output efficiency and brightness (and building an electrically-pumped laser is difficult).

Fullerene Production. Researchers at Rice University announced the first creation and isolation of macroscopic quantities of C_{60} and C_{70} molecules and other less-common fullerenes by placing a carbon arc inside a partially evacuated inert atmosphere (Helium gas at around 1/6 of an atmosphere) and supplying a high voltage. However, there turned out to be a problem with using arc lamps to produce fullerenes in that, as the size of the arcs increased, the yield relative to total soot vaporization decreased. This led to the consideration of using highly concentrated sunlight. Sunlight on earth has a relatively low UV content and mirrors can be made less reflective at lower wavelengths, making it a promising source to produce fullerenes. Using solar flux to produce small amounts of fullerenes was demonstrated simultaneously by both researchers at Rice University and researchers at NREL. The method at NREL used a nonimaging secondary CPC in conjunction with the High Flux Solar Furnace. More recent work is underway to develop mass-production techniques. The scalability of solar as opposed to small scale arc lamp systems may make this the preferred method of fullerene production.

Solar Processing of Materials. Ideally, concentrated sunlight can cause materials to reach equilibrium temperatures approaching those found on the sun's surface (5,800 K). This allows solar to cover a wide range of applications at all temperatures below this level. The high fluxes also lead to extremely high heating rates in non-equilibrium setups because the heating rate is proportional to the incident flux minus the reradiation losses, which are small for low temperatures. Surfaces of materials can be superheated to induce chemical reactions that modify the properties and composition on a material's surface while leaving the bulk material unchanged.

Dish-thermal Applications (Reflecting Trumpet Secondary) A project is being carried out by he University of Chicago to design a practical trumpet secondary concentrator to be use in combination with a faceted membrane primary concentrator for dish-stirling applications. This is a retrofit design for a dish which was originally designed as a single stage and so it cannot attain the full power of a fully optimized two stage concentrator. Nevertheless, preliminary ray trace studies show that the addition of a small trumpet to the receiver aperture will allow a reduced aperture size and corresponding lower thermal losses at the operating temperature of 675° C.

Solar thermal Applications of High-Index Secondaries. There is interesting research at the Weizmann Institute of Science (WIS) in Israel, studying the use of large-scale dielectric secondary concentrators and an efficient extractor tip to create high-temperature gas turbine engines. A summary of their system is given in Ref. [9], but has relatively little on their extractor design. More information on the extractor tip operation can be found in Ref. [8]. The use of high-index concentrators with TIR reflection conditions (no losses from reflection that occur on metal surfaces) minimize optical losses in the system and increases the concentration limit by n^2. In general, the use of a higher-index material to form the aperture of a gas turbine will not give higher operating temperatures. This is because the reradiation is proportional to n^2 times the area of the secondary exit aperture, which normally cancels the n^2 gain in concentration obtained by using higher-index materials. All gas turbines operate at temperatures much less than the sun's (6000 K) and therefore, the spectrum of reradiation is considerably red-shifted into the infrared (IR) region. By applying selective coatings onto the dielectric concentrator and extractor optics, one may prevent IR radiation from reradiating and it may be possible to reduce heat losses inside high-temperature electrical generation systems. Research is in progress at the Weizmann Institute of Science in Israel [9]to study the coupling of dielectric secondaries with gas turbines. They use a 6-sided extractor tip to let light out of the high-index secondary and into the high-temperature gas environment of the turbine (n=1).This is another possible use of high-index secondaries other than end-pumping solid-state laser crystals.

<u>Using Highly Concentrated Sunlight in Space</u> The techniques of nonimaging optics are particularly valuable in space or lunar environments where the use of solar thermal energy has obvious advantages. Earlier preliminary studies have explored this concept for the production of cement from lunar regolith and for solar thermal propulsion in space. For example, extremely high temperatures, in the range 1700 to 1900°C, are necessary for the production of cement from lunar minerals. Such temperatures, will in turn require very high levels of solar flux concentration. Energy budgets for the support of permanent manned operations on the lunar surface are expected to be limited. For high temperature thermal (i.e. >300° C) end uses, direct solar energy has obvious advantages over most other practical power sources. Conventional combustion processes are clearly impractical and conversion of electricity (either solar or nuclear generated) to high temperature heat represents a very wasteful use of high quality energy. On the other hand solar radiation is abundant and non-depletable. Most importantly, it is readily converted to heat with high efficiency, although at high temperatures this requires high concentration as will be discussed below.

Earlier work illustrated the feasibility of some particular two-stage configurations and indicated that the corresponding solar thermal conversion efficiency can be about 2.5 times that of the corresponding conventional design at 1500°C. A preliminary design configuration for such a high flux nonimaging solar concentrating furnace for lunar applications was proposed . It employs a tracking heliostat, a fixed, off-axis, two-stage concentrator with a long focal length utilizing a nonimaging trumpet or CPC type secondary deployed in the focal zone of the primary. An analysis of the benefits associated with this configuration employed as a solar furnace in the lunar environment shows that the thermal conversion efficiency can be about 3 to 5 times that of the corresponding conventional design at 2000°C. Furthermore this configuration allows several other advantageous practical design options in addition to high performance. For instance, the furnace itself and associated support structure and equipment need not shade the primary collecting aperture and spherical or faceted primaries may be able to be used.

Solar thermal propulsion systems in space will require very high temperatures to generate necessary levels of thrust by the direct solar heating and resulting expansion and expulsion of the propellent material. The generation of such temperatures, in the range 1400°C to 2200°C, will in turn require very high levels of solar flux concentration. In practice, to attain such levels it may be useful and perhaps even necessary to incorporate some form of ideal or near ideal nonimaging concentrator.

DISCUSSION

Applications of the techniques of nonimaging optics in the design of solar thermal concentrators has resulted in significant performance improvements in conventional short focal length dish concentrators, dramatic changes in the approach to solar furnace design, and the establishment of new solar flux concentration records in air and in refractive media. These accomplishments in just over ten years of active experimental development are indications of what can be achieved with these powerful methods. The wide variety and range of applications make this a very exciting field. It extends the bounds of solar energy research into solar manufacturing and even moves us in and into outer space.

List of References
1) Cooke, D., Gleckman, P., Krebs, H., O'Gallagher, J., Sagie, D., and R. Winston, 'Brighter than the Sun", *Nature* **346**, 802, 1990.

2) Welford, W. and R. Winston (1989), High Collection Nonimaging Optics, Academic Press, New York.

3) Welford, W. and R. Winston (1980), "Design of Nonimaging Concentrators as Second Stages in Tandem with Image Forming First-Stage Concentrators," *Appl. Opt.* **19**(3), 347-351.

4) O'Gallagher, J., Winston, R., and A. Lewandowski (1993), "The Development of Two-stage Nonimaging Concentrators for Solar Thermal Applications,"Proceedings of the American Solar Energy Society Annual Conference, Washington, D.C, 203-209.

5) Ning, Xiaohui, O'Gallagher, J. and R. Winston (1987), "The Optics of Two-Stage Photovoltaic Concentrators with Dielectric Second Stages," *Applied Optics,* **26**, 1207.

6) Lewandowski A., Bingham, C., O'Gallagher, J., Winston, R., and D. Sagie (1991), "Performance Characterization of the SERI High Flux Solar Furnace," *Solar Energy Materials* **24**, 550-563.

7) Jenkins, D., Winston, R., Bliss, J., O'Gallagher, J., Lewandowski, A. and C. Bingham (1996a), "Solar Concentration of 50,000 Achieved with Output Power Approaching 1 kW," submitted to *J. Sol. Energy Eng.*

8) Karni, J., Ries, H., Segal, A., Krupkin, V., and A. Yogev (1994), "Delivery of Radiation for a Transparent Medium," Israel Patent 109,366 and international patent application PCT/US95/04915.

9) Karni, J., Ries, H., Segal, A., Krupkin, V., and A. Yogev (1995), "The DIAPR: A High-Pressure, High-Temperature Solar Receiver," Intl. Solar Energy Conf., Hawaii, 591-596.

10) Jenkins, D. and R. Winston (1996), "Integral Design Method of Nonimaging *Optics,*" accepted for publication in *J. Opt. Soc. Am. A.*

11) Krupkin, V., Kagan, Y., and A. Yogev (1993), "Non Imaging Optics and Solar Laser pumping at the Weizmann Institute,"Nonimaging Optics: Maximum Efficiency Light Transfer II, Proceedings SPIE 2016, 50-60.

LOCALIZATION OF ENERGY ON THE MOLECULAR SCALE

Katja Lindenberg and David W. Brown

Department of Chemistry and Biochemistry and Institute for Nonlinear Science
University of California, San Diego
La Jolla, CA 92093-0340, U.S.A.

ABSTRACT

We discuss the spontaneous localization of vibrational energy in translationally invariant anharmonic chains at finite temperatures. In addition to the familiar energy-driven coherent mechanisms, which are rapidly degraded by thermal fluctuations, we identify the entropy-driven phenomenon we call "stochastic localization", within which we include a number of characteristics of soft anharmonic oscillators in thermal equilibrium. Principal among these are a tendency for soft oscillators to spend more time at higher energies than comparable harmonic oscillators, and for high-energy fluctuations in soft oscillators to persist for longer times than lower-energy fluctuations, leading to a tendency for energy fluctuations to be organized into "bursts" separated by intervals of relative quiet. We illustrate the effects of stochastic localization on a bistable impurity embedded in a chain of soft oscillators by comparing it to an impurity embedded in a harmonic chain. Effects on transition rates at a given system energy can be quite dramatic.

The spontaneous localization of mobile vibrational energy in molecular materials as an energy-focusing mechanism has long been an intriguing idea. This possibility has arisen, for example, in the context of materials in which such localization and/or transport may in turn lead to switching and other thresholding phenomena, detonation, chemical reactions, or local melting and other deformational effects. The mechanisms whereby energy in low-frequency modes can be transferred to higher energy modes (e.g. from vibrational to electronic) pose many interesting questions. For example, consider the events leading up to the regime where chemistry begins following a mechanical shock. Because the principal effect of an impinging shock is to promptly compress a material passing under it, energy is first delivered into low-lying vibrational modes associated with volumetric compression; these include the acoustic modes associated with translations of the center of mass of a unit cell, librational modes associated with rigid-body rotations of principal unit cell constituents, and the lowest-lying optical modes associated with relative translations of unit cell constituents. On the other hand, chemical reactions are associated with deformations of individual molecules and with their electronic excitations. Therefore, understanding such chemical reaction problems leads us to focus on the dynamics of their low-lying vibrational mechanical precursors and their coupling to higher energy modes.

Spontaneous energy localization in molecular materials may arise in qualitatively different ways. The most thoroughly studied energy localizing mechanism is static disorder through compositional variability or through the presence of defects. This mechanism is ubiquitous and quite well understood, and is *not the subject of our work*. While disorder promotes energy localization, it inhibits energy transport. We are interested in localization mechanisms that can coexist, at least in principle, with transport mechanisms. Such energy-localizing mechanisms arise even in translationally invariant aggregates (e.g., even nearly defect-free energetic materials are detonable) and are made possible by *anharmonicities*. The very localization of energy

in turn may drive the system (at least locally) into even more nonlinear regimes.

In the absence of thermal fluctuations a wide variety of translationally invariant anharmonic systems are capable of supporting long-lived, localized excitations under appropriate conditions. In this characterization we include not only completely integrable systems that support robust, spatially coherent, infinitely-long-lived solitons and solitary waves, but also a number of systems that support localized excitations for experimentally relevant times. Although many such systems have been identified in principle, the experimental observation of molecular solitons has been less successful. There are several reasons for this difficulty: (1) Few practical situations approach a degree of idealization consistent with the existence of infinite-lived or even very long-lived excitations such as solitons. A particular challenge in this regard is arriving at a practical and quantitative characterization of a "meaningful lifetime." (2) It may be difficult to create initial conditions that lead to soliton-like behavior; this particular statement will be illustrated below. (3) Most experimental techniques available for probing soliton structure are indirect and nondiscriminating in the sense that bulk properties of materials are probed; thus, most measurements average signals over substantial volumes of space thus simultaneously including coherent and incoherent motions and presenting serious challenges to deconvolution.

Thermal fluctuations tend to degrade the careful *energy-driven* balance that leads to coherent localization. On the other hand, we have recently identified an *entropy-driven* localization mechanism that we have called *stochastic localization* [1]. This mechanism, which occurs in soft anharmonic oscillators, is more robust than energy-driven localization. Below we describe the origin of this localization and some of its signatures. Its practical observation and/or importance remain to be ascertained.

Consider a chain of N oscillators labeled $n = 1, 2, \cdots, N$ with periodic boundary conditions ($N + 1 \equiv 1$). Each oscillator is subject to an on-site potential $V(x_n)$ and to harmonic nearest-neighbor interactions. The Hamiltonian of the system is

$$ H\{\dot{x}, x\} \;=\; \sum_n \left[\frac{1}{2}\dot{x}_n^2 \;+\; \frac{1}{2}c^2(x_n - x_{n-1})^2 \;+\; V(x_n) \right] . \tag{1} $$

We consider two types of chains. In one the on-site potential is harmonic with unit frequency, $V(x) = x^2/2$. This we call the *harmonic chain*. In the other the on-site potential is soft anharmonic,

$$ V(x) \;=\; \frac{1}{2}\frac{x^2 \;+\; \alpha x^4}{1 + x^2}, \tag{2} $$

with $\alpha < 1$. This we call the *anharmonic chain*. Note that the harmonic chain is subsumed in Eq. (2) if we set $\alpha = 1$. If we set $\alpha = 0$ the on-site potential saturates and the oscillators can "run away." We will therefore always take $\alpha > 0$.
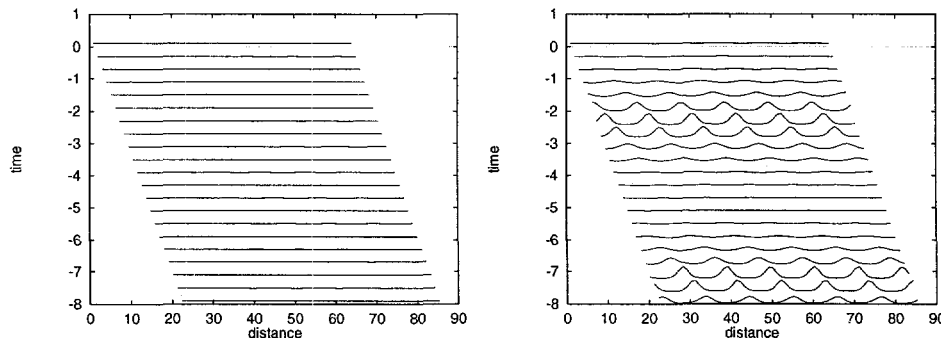

Figure 1: Energy density profile for harmonic (left panel) and anharmonic (right panel) chains with modulated initial condition.

The harmonic chain has N normal modes whose behavior is clearly understood. The anharmonic chain, on the other hand, does not have normal modes and in fact supports soliton and other solitary wave solu-

tions. An example that illustrates this behavior is shown in Fig. 1. The figure shows the result of initializing each chain of 64 oscillators with a nearly-uniform initial energy distribution upon which is imposed a weak spatially-periodic modulation. The left panel is the harmonic chain, while the right panel shows the anharmonic chain. The chains have been "opened" for graphing purposes. The vertical axis in each case indicates the local energy density, the horizontal axis indicates distance, and successive offsets indicate the progression of time. The modulation in the harmonic chain persists in time, but is hardly visible on the scale shown. On the other hand, the modulation in the soft anharmonic chain grows periodically in time, transforming the original nearly-uniform energy distribution into a train of pulses, each of which spans a number of unit cells within which a several-fold amplification of the original energy density is achieved for a non-trivial interval of time [2]. The rather coherent concentration of energy achieves local deformations that may assist in the initiation of chemistry [3, 4]. The dramatic focusing in this particular case is a transient phenomenon ("instability") that is eventually degraded.

We are ultimately interested not only in the performance of such a medium at zero temperature, where nonlinear collective excitations that lead to energy localization are often stable (at least in some parameter regimes), but also at finite temperatures, where such coherent collective excitations must compete with thermal fluctuations.

We have recently identified an energy-localizing mechanism that is *driven* by thermal fluctuations, that is, it is entropy driven rather than energy driven [1]. This mechanism, which we call *stochastic localization*, is even more general and ubiquitous than other energy localization mechanisms that have been proposed for regular molecular aggregates. Stochastic localization does not require spatial coherence and is robust in the face of thermal effects — indeed, it can be argued to be in competition with forces that foster spatial organization.

In order to describe stochastic localization, consider first a *single* oscillator described by the Hamiltonian $H\{\dot{x}, x\} = \frac{1}{2}\dot{x}^2 + V(x)$, in which $V(x)$ is the on-site potential introduced earlier. When such an oscillator is in contact with a thermal bath at temperature T, a number of simple thermodynamic arguments applied to an ensemble of such independent oscillator immediately lead to the following conclusions:

1. The average energy of a soft anharmonic oscillator is higher than that of a harmonic oscillator at a given temperature: they share the same average kinetic energy at a given temperature, but the soft oscillator has greater excursions and therefore a higher potential energy.

2. The energy fluctuations in a soft anharmonic oscillator are larger than those of a harmonic oscillator at the same temperature. This conclusion is easily reached from a simple analysis of the specific heat which is directly connected to these fluctuations.

3. In an ensemble of harmonic oscillators (or in a single oscillator over time) half of the total energy on average is in kinetic form and half in potential form. In an ensemble of soft oscillators, on the other hand, on average a greater fraction of the total energy is in potential form.

4. The previous item immediately leads to the conclusion that a high energy fluctuation in a soft anharmonic oscillator persists for a longer time than does an equal fluctuation in a harmonic oscillator. This is due to the fact that the rate of energy dissipation is directly proportional to the *kinetic* energy.

All of the foregoing considerations point to the notion of statistical localization, that is, *a spatial and temporal localization of energy in anharmonic oscillators*. This localization is entropy-driven and incoherent: it comes about because the density of states of a soft anharmonic oscillator increases with energy so that it is entropically favorable for the system to concentrate higher energies in some members of the ensemble (and lower energies in others) than it would in an ensemble of harmonic oscillators, where the favorable distribution is more uniform. Furthermore, high-energy fluctuations survive for a longer time in the anharmonic chain.

What happens when oscillators are connected as a network such as described by the Hamiltonian (1)? The effect of the nearest neighbor interactions is to drive neighboring oscillators toward the same phase and thus to establish coherence on the smallest spatial scale. Dynamically, this local drive toward spatial coherence has the effect of dispersing any localized energy distribution, since such a distribution constitutes a *deviation* from perfect alignment. The main dynamical consequence of building spatial coherence in vibrational systems is *dispersion*. Thus at zero temperature two opposing tendencies coexist: that of the soft anharmonicity to *increase inhomogeneity*, and that of the coupling to lead to the *dispersion* of energy

81

and hence to a *decrease in inhomogeneity*. Optimal solutions achieve some degree of balance between these opposing tendencies, often giving rise to solitary wave solutions and their idealization in the concept of the soliton [2]. These optimal solutions may or may not survive the effects of thermal fluctuations and dissipation. On the other hand, thermal fluctuations bring with them the complementary effect of stochastic localization. This localization mechanism becomes stronger with increasing thermal fluctuations, but the coupling between oscillators acts to further redistribute energy from a "hot" oscillator to its neighbors. It is difficult to know what the final balance might be. Although both the coherent and the incoherent localization mechanisms are a direct consequence of the (softening) anharmonic character of the oscillators, they are in a sense opposite to one another and also to the dispersive action of increased coupling.
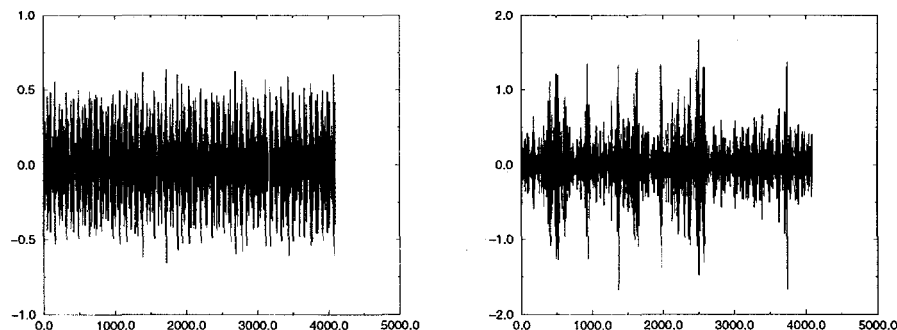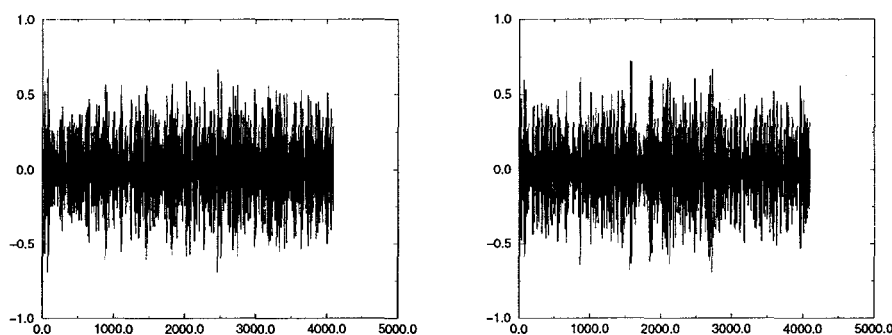

Figure 2: Position of oscillator 55 as a function of time in the harmonic chain (left panel) and the anharmonic chain (right panel) of Figure 1. Note the scale differences.
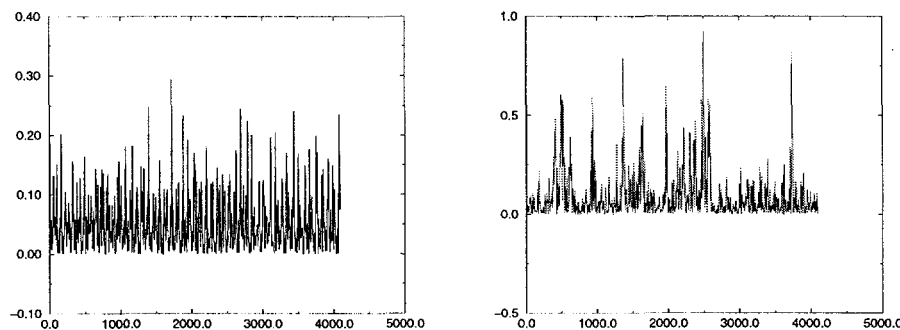
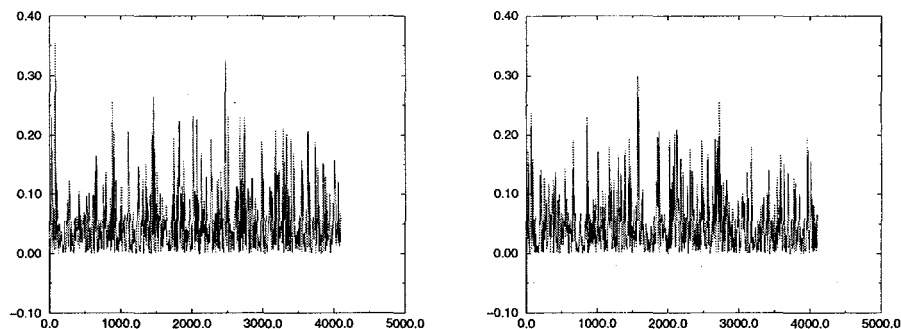Figure 3: Energy of oscillator 55 as a function of time in the harmonic chain (left panel) and the anharmonic chain (right panel) of Figure 1. Note the scale differences.

At this time most of our available information comes from simulations. We have carried out simulations on harmonic and anharmonic chains (the latter with $\alpha = 0.05$). The value of the dispersion parameter c plays a central role in determining the nature of the ultimate self-consistent state in the absence of thermal fluctuations; large values tend to result in broad solitary waves spanning many lattice sites, and small values

tend to result in compact localized vibrations that may be "pinned" to particular lattice sites [5]. In our work we have mostly used the value $c = 0.5$ (this is also the value used to generate Fig. 1), which besides being "intermediate" (the allowed range is $c \in (0, 1)$), is motivated by consideration of the actual dispersion relations of low-lying librations in certain organic molecular crystals [6]. The values of c typically chosen for the study of anharmonic arrays designed to exhibit nonlinear behavior are usually much smaller, of the order of 10^{-2} [7].

In Fig. 1 we showed the evolution of chains of 64 coupled oscillators with an initial condition that led to clear coherent focusing in the anharmonic chain. In Figs. 2 and 3 we show for exactly the same systems a number of other features of these chains. The first panel in Fig. 2 shows the trajectory of one of the oscillators (number 55) in the chain as a function of time, and the second panel shows the trajectory of this oscillator in the anharmonic chain. Although the quality of coherence is a bit less clear than in Fig. 1, the differences are evident. They are also evident in Fig. 3, which shows the energy of this oscillator in the chains as a function of time.

Figure 4: Position of oscillator 55 as a function of time in the harmonic chain (left panel) and the anharmonic chain (right panel). The chains have the same initial energy as in Figure 2 (0.1 per oscillator) but distributed randomly.

Figure 5: Energy of oscillator 55 as a function of time in the harmonic chain (left panel) and the anharmonic chain (right panel). The chains have the same initial energy as in Figure 3 but distributed randomly.

The importance of the initial condition is evident when we compare these figures to those shown in Figs. 4 and 5. In these four panels we show exactly the same oscillator in exactly the same chains with exactly the same total energy, but now the energy is initially randomly distributed. Although this is a microcanonical (fixed energy) system, in this set of figures the systems behave essentially as they would in thermal equilibrium. Now the energy is distributed quite uniformly in both chains, and there is no evidence of coherent energy focusing. The initial energy is too low to show the effects of stochastic localization - the average energy per oscillator is 0.1, which places it near the bottom of the on-site potentials where both potentials are very similar. Again, we stress the importance (and difficulty) of creating the proper initial condition in order to observe the effects of coherent localization.

How might one observe stochastic localization and/or the way it may coexist with coherent localization mechanisms? A number of possible signatures come to mind. One is to connect the chains to a heat bath of sufficiently high temperature, so that energies where the harmonic and anharmonic potentials differ substantially come into play. The two panels in Fig. 6 show such a case. It is difficult without further analysis to conclude whether or not there is a substantial difference in the texture of these two chain histories – the sharp persistent ridge in the anharmonic chain differs from those in the harmonic chain in a number of ways, including the fact that the anharmonic ridge is clearly mobile and keeps its integrity during the entire time history shown in the figure.
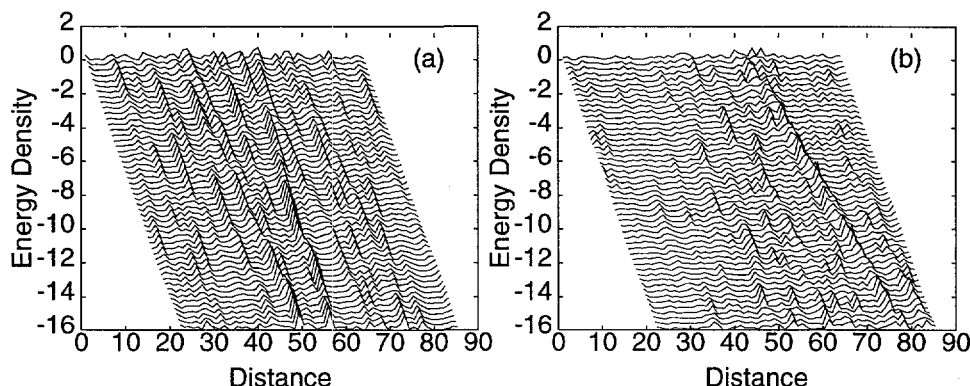

Figure 6: Time dependence of the energy density in a chain of oscillators evolving according to (1) with $c = 0.5$. The chain is in contact (via appropriate Langevin terms) with a heat bath at temperature 0.5. Vertical axes represent energy, horizontal axes represent distance along the chain of 64 sites. Time increases from top to bottom. Left panel: harmonic chain; right panel: anharmonic chain.

Another probe of stochastic localization, more directly related to our goal of identifying localization mechanisms that might trigger other events, is to place a bistable "impurity" in the chain. In this case our chain consists of 64 oscillators (harmonic or anharmonic) connected as before and one bistable on-site potential of the form

$$V(x) = V_0 \left(\frac{x^4}{4} - \frac{x^2}{2} \right) , \tag{3}$$

also connected via harmonic springs to its neighbors (we label this particle number 65 and connect it to its neighbors, oscillators 1 and 64, by the same harmonic springs as connect the other oscillators). If we think of this bistable system as a configuration coordinate, then one of the wells might represent one configuration (or "reactant") and the other another configuration (or "product"). The characteristic frequencies of the bistable impurity are chosen to fall within the band of frequencies of the chain so that any energy localization cannot be ascribed to an energy mismatch as occurs in many disordered systems. In our simulations we take $V_0 = 0.75$. If localization is observed, it is certainly due to the anharmonicity of the chain; if it occurs at sufficiently high "temperature," then it is due to stochastic localization rather than coherent localization.

In Fig. 7 we show a typical trajectory of the bistable system in a harmonic chain (left panel) and anharmonic chain (right panel) with a random initial distribution of energies (microcanonical system). The average energy per oscillator is 0.23. We point to the following difference in texture: in the harmonic panel the impurity tends to oscillate in one of the bistable wells (either around -1 or around 1) with single passages

from one to the other. If the impurity gains enough energy to make the transition, it loses it quickly, remains in the other well for a while, and then gains sufficient energy to cross again. In the anharmonic panel, on the other hand, if the bistable particle gains enough energy it tends to *retain* it for a long time, thus oscillating back and forth at a high energy above the barrier separating the wells. Once this energy is lost, the bistable particle remains rather cold for a while, that is, its oscillations have a smaller amplitude than those of the harmonic system. This is the signature of stochastic localization: the anharmonic chain causes the impurity to experience persistent hot and cold periods relative to the harmonic chain. In Fig. 8 we show the phase space portrait of the bistable system in the two cases. The right panel has a greater concentration of both cold and hot trajectories than the left. In Fig. 9 we show another example of the trajectories of the bistable impurity; here the energy per oscillator is 0.23. Clearly, the transition rate statistics in the two chains are quite different.
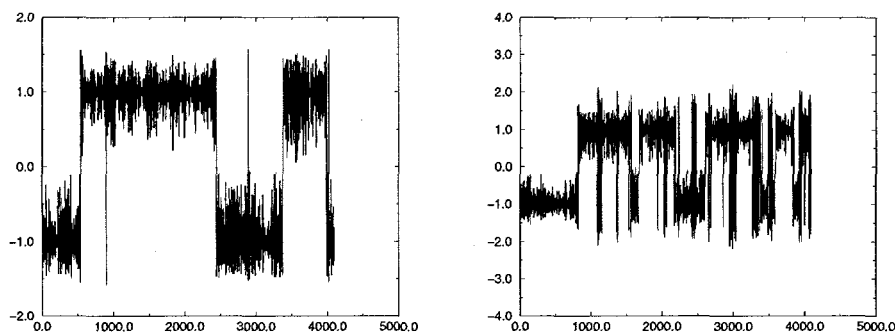
Figure 7: Time dependence of the trajectory of a bistable impurity in a chain, with initial energy 0.23 per site. Left panel: harmonic chain; right panel: anharmonic chain. Note the scale differences.
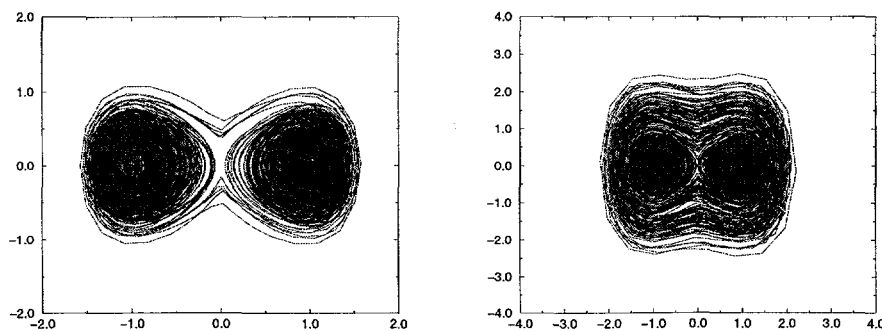
Figure 8: Phase space portrait of a bistable impurity in a chain, with initial energy 0.23 per site. Left panel: harmonic chain; right panel: anharmonic chain. Note the scale differences.

We have compared and contrasted two mechanisms for energy localization in translationally invariant anharmonic chains. The more familiar one is energy driven and leads to coherent localization in the form of solitons, solitary waves, and other such coherent structures. These structures are sensitive to (and usually disappear in the presence of) thermal fluctuations. The other, more robust, mechanism of energy localization in (soft) anharmonic chains relies on the presence of thermal fluctuations and is entropy-driven. We
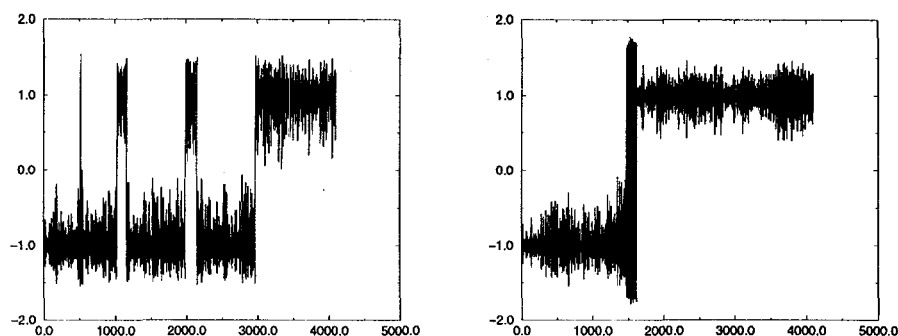
Figure 9: Time dependence of the trajectory of a bistable impurity in a chain, with initial energy 0.20 per site. Left panel: harmonic chain; right panel: anharmonic chain.

discussed the subtleties involved in observing and discriminating between these mechanisms. We continue to develop these ideas in classical systems and have made some preliminary progress in quantum systems, where translational invariance places even greater burdens on the stationary states of the system [8].

ACKNOWLEDGEMENT

REFERENCES

[1] D. W. BROWN, L. BERNSTEIN, and K. LINDENBERG, "Stochastic Localization," *Phys. Rev. E* **54**, 3352 (1996).

[2] G. B. WHITHAM, *Linear and Nonlinear Waves*, John Wiley & Sons, New York (1974); R. K. DODD, J. C. EILBECK, J. D. GIBBON, and H. C. MORRIS, *Solitons and Nonlinear Wave Equations*, Academic Press, New York (1982); A. NEWELL, *Solitons in Mathematics and Physics*, SIAM, Philadelphia (1985).

[3] R. A. MARCUS and N. SUTIN, *Biochim. et Biophys. Acta* **811**, 265 (1985), and references therein.

[4] L. SANCHE, *IEEE Trans. Elec. Insulation* **28**, 789 (1993), and references therein. lattice sites

[5] R. S. MACKAY and S. AUBRY, "Proof of existence of breathers for time-reversible or Hamiltonian networks of weakly coupled oscillators," *Nonlinearity* **7**, 1623 (1994).

[6] A. M. MICU, D. DURAND, M. QUILICHINI, M. J. FIELD, and J. C. SMITH, "Collective vibration in crystalline l-alanine," *J. Phys. Chem.* **99**, 5645 (1995).

[7] D. HENNIG, K. O. RASMUSSEN, and G. P. TSIRONIS, "Breatherlike impurity modes in discrete nonlinear lattices," *Phys. Rev. E* **52**, R4628 (1995).

[8] D. W. BROWN and K. LINDENBERG, "Looking for soliton signatures in polaron Bloch states," to appear in *Physica D* (1997).

QUANTITATIVE PHOTOGRAPHY OF INTERMITTENCY IN SURFACE WAVE TURBULENCE

W.Wright, R. Budakian, S.J. Putterman

Physics Department, University of California, Los Angeles, CA 90095

ABSTRACT

At high amplitudes of excitation surface waves on water distribute their energy according to a Kolmogorov type of turbulent power spectrum. We have used diffusing light photography to measure the power spectrum and to quantify the presence of large structures in the turbulent state.

INTRODUCTION

One of the key problems of science and engineering is to understand the fate of energy which is injected into a fluid so as to drive it very far from equilibrium. As the energy flows through phase space it experiences a competition between randomization and structure formation which are issues that come into play in the study of turbulence. The properties of turbulent flow are of importance in phenomena ranging from turbomachinery to airplane design, to weather prediction. A good perspective on the problem of turbulence is provided by the following three quotes:

> "Big whorls have little whorls
> Which feed on their velocity;
> And little whorls have lesser whorls,
> And so on to viscosity
> (in the molecular sense)"

> "The wind comes in gusts."

> "I am an old man now and when I die and go to heaven there are two matters on which I hope for enlightenment. One is quantum electrodynamics and the other is the turbulent motion of fluids. And about the former I am really rather optimistic."

The first quote is due to Richardson (1926)[1] and expresses the concept of the turbulent cascade. Energy which enters a fluid at long wavelength scatters from itself to generate motion on shorter and shorter wavelengths. This is the way in which turbulent

nonlinear interactions create a randomization of the input energy. However, turbulence is not so simple. Turbulence is not merely scaled up thermal noise. In the midst of the random motion there can appear unexpected concentrations of energy, which are typically surfaces on which the dissipation is concentrated[2]. This "intermittency" is the basis for the second quote which has been attributed to Landau. The difficulties connected with the interplay between intermittency and the cascade are pinpointed by the third quote due to Sir Horace Lamb[3].

Looking back at this prophetic remark we can note the mathematical structure that has been developed to explain 'qed' and marvel at the lack of progress in defining, probing, and solving the problem of turbulence. This situation persists despite the huge interest in 'chaos' and the experimental opportunities openned up by modern technology. We propose that the continuing validity of Lamb's quote is due in part to the inability of experimentalists to provide quantitative measurements of the wavenumber or 'k' spectrum of turbulent motion. Only from the 'k' spectrum can one diagnose the complex modal structure of high amplitude motion. As we will demonstrate below such measurements provide a quantification of intermittency and randomness in turbulence and they form the basis for advances in the analytic theory.

The physical system which we have used to gain insight into turbulence consists of capillary waves that run around on the surface of a fluid. At low amplitude the principle of superposition applies and the waves run through each othe. But at high amplitudes nonlinear terms cause the waves to scatter. This exchange of energy eventually leads to wave turbulence.

EXPERIMENT

Figure 1 shows the apparatus that we have used to excite and measure the large amplitude distortions of a fluid surface[4]. A vibration exciter oscillates a container of fluid in the vertical direction at sufficient amplitude that instabilities determined by the Matthieu equation come into play. The resulting surface motion is made visible by suspending into the water a .04% solution of polyballs. This concentration is sufficiently dense that light traveling through the water is so strongly scattered that it diffuses. A charge coupled device (CCD) records the light to exit the fluid. Typically the surface is broken up into one million pixels [1024x1024] where each pixel is capable of recording a dynamic range of 65,000 gray scales [or 16 bits]. This image is converted into the surface height with the help of a calibrated measurement of the amount of light to exit the surface as a function of fluid depth. The deeper the fluid the smaller is the amount of light to make it to the surface at that location.

At low amplitudes of excitation the motion is regular and exhibits the square wave patterns so characteristic of parametrically excited ripples[5]. At high amplitudes there is a transition to stochastic motion characteristic of the turbulent state that we wish to understand. Renderings of the data for low and high amplitude motion are shown in Figure 2. The broad band power spectrum of high amplitude motion [converted to a function of ω] is shown in Figure 3b. The slope of the observed spectrum [on a log-log plot] is close to that predicted by Kolmogorov scaling laws [6].

Theories which are based upon a random phase approximation yield a power spectrum in agreement with the Kolmogorov dimensional analysis and of course also yield a description of turbulence that is devoid of intermittency. Since phase is a physical quantity of importance equal to power [or amplitude squared] we have used the instantaneous photos to investigate the phase coherence, if any, of the turbulent state. To do this we digitally filtered the photo to include only the contributions from a range of wavelengths. In this case those wavelengths corresponding to the frequency range 373Hz to 429Hz [as indicated on Figure
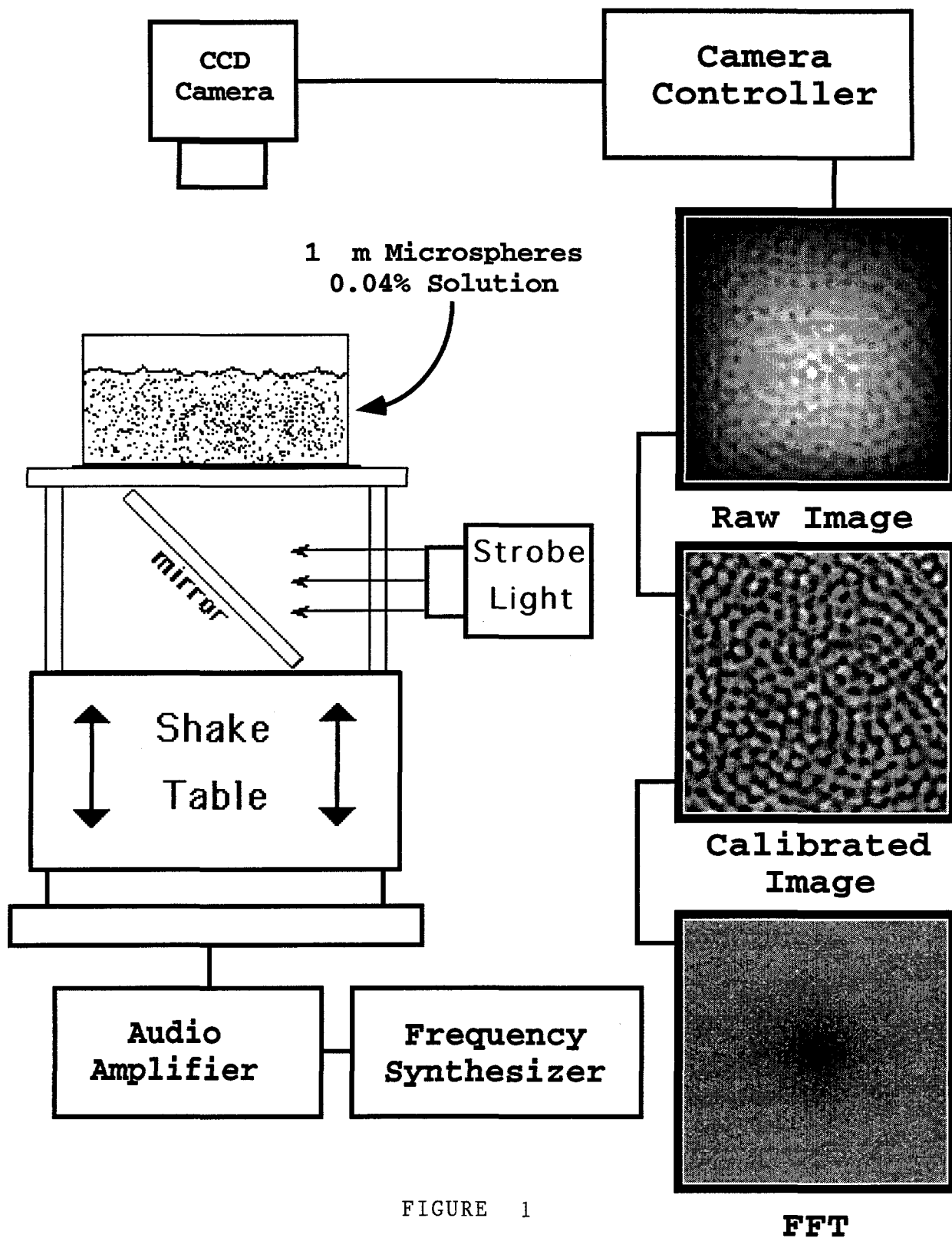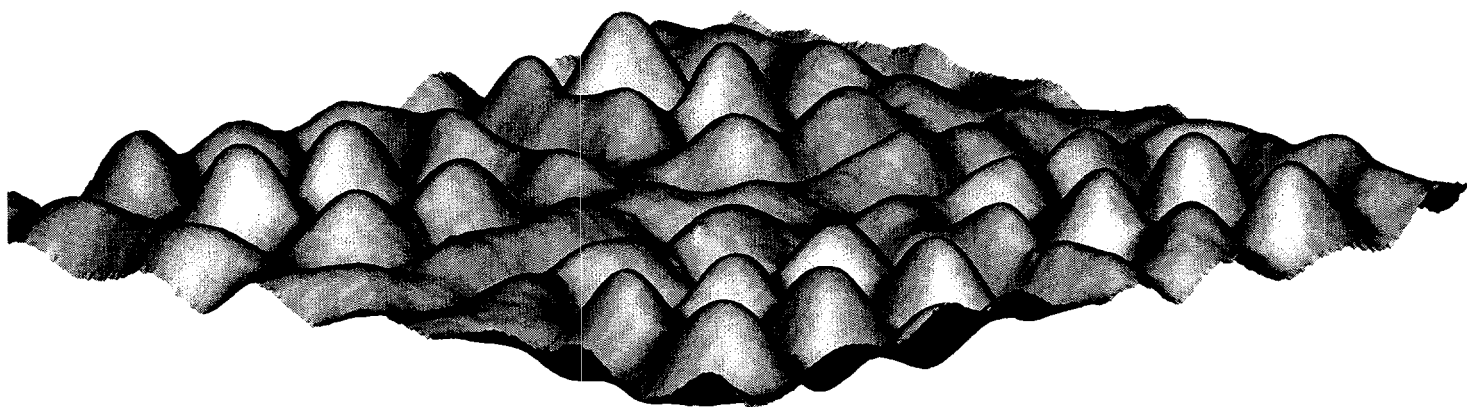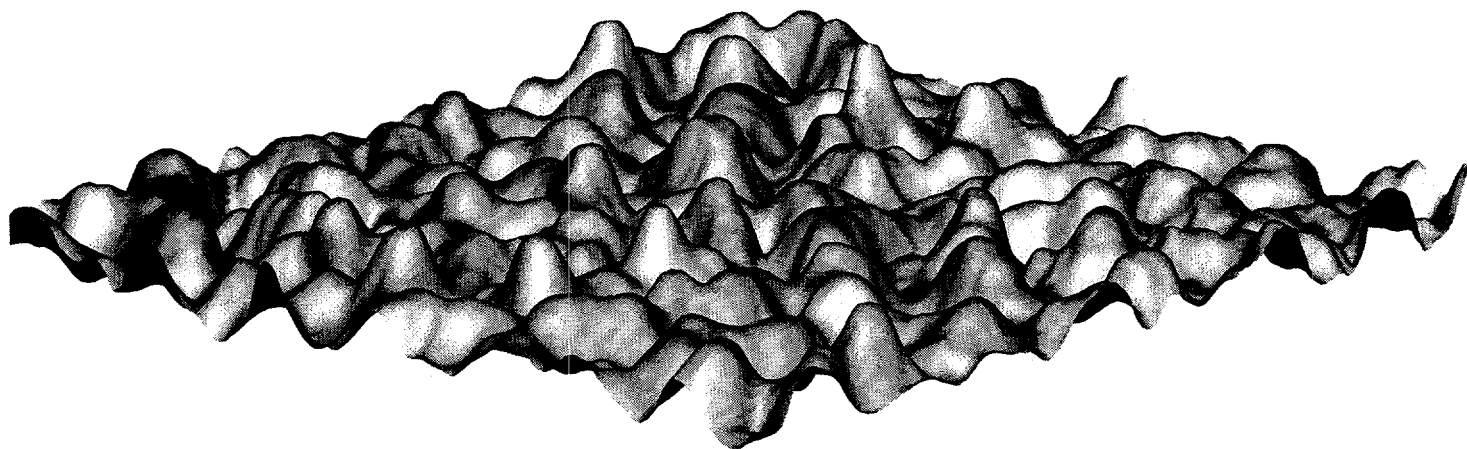
CCD Camera

Camera Controller

1 m Microspheres
0.04% Solution

mirror

Strobe Light

Shake Table

Audio Amplifier

Frequency Synthesizer

Raw Image

Calibrated Image

FFT

FIGURE 1

FIGURE   2

(a)

number

size of structure

number

2x10⁴

displacement (mm)
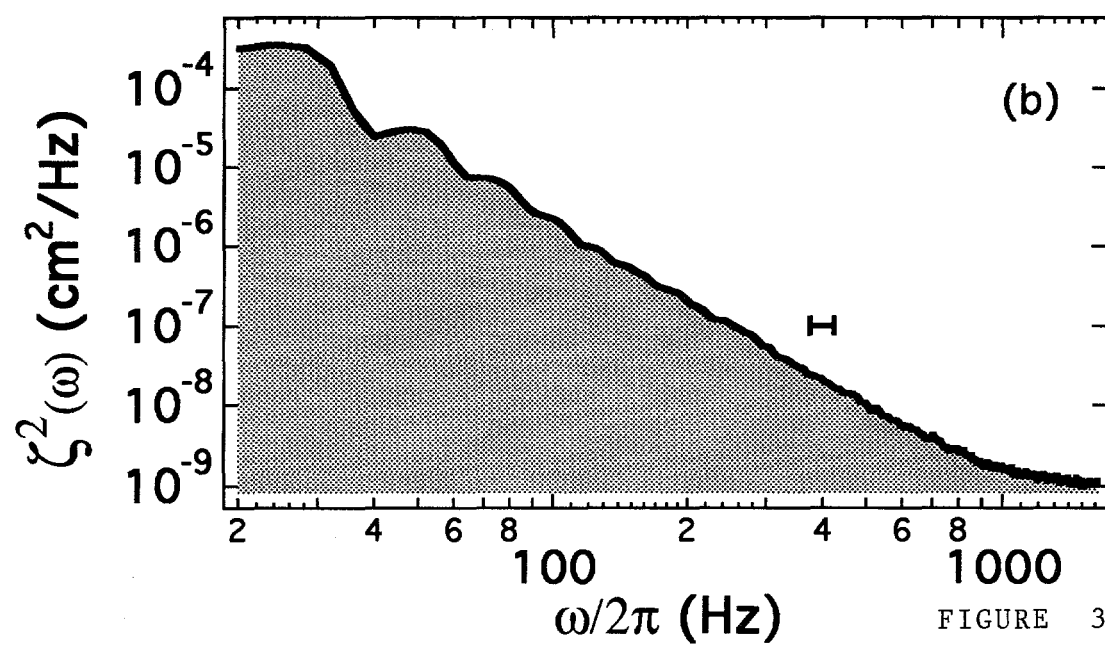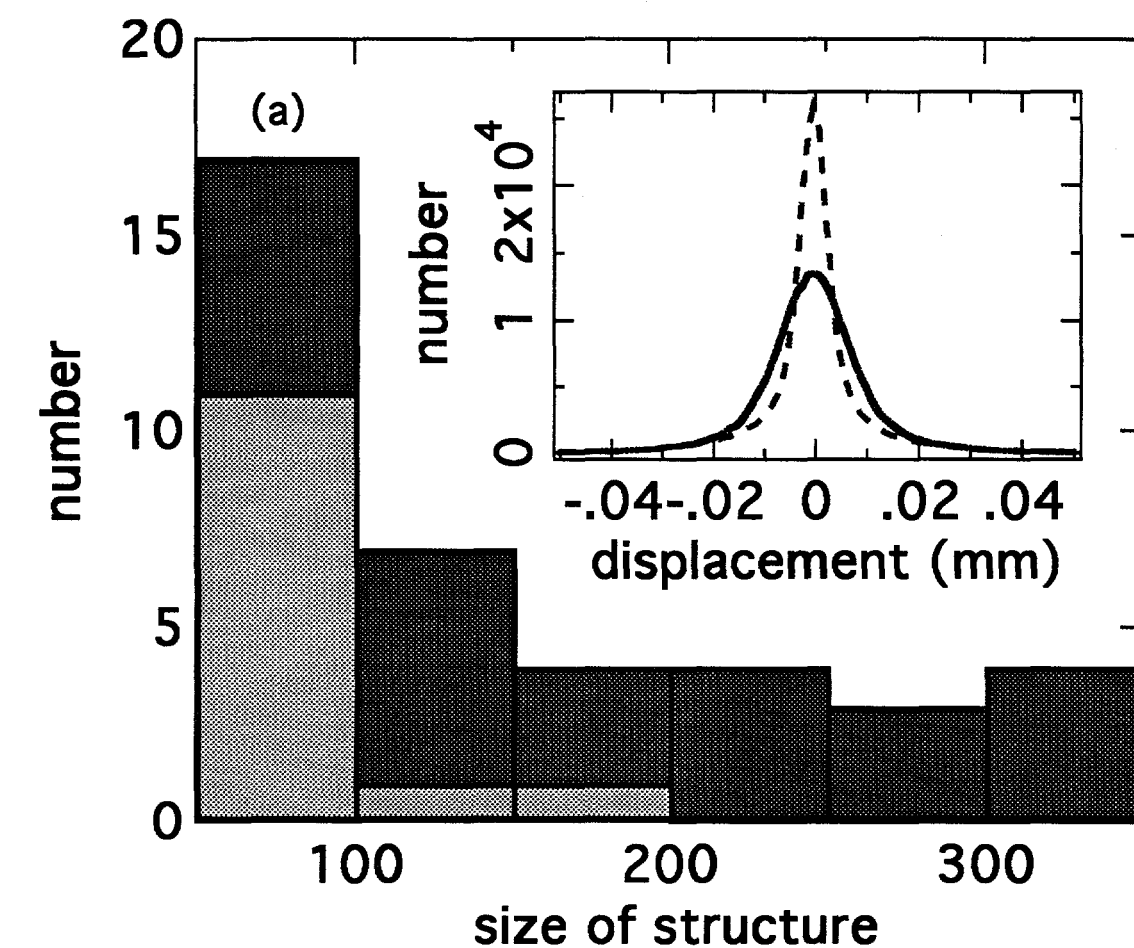
(b)

$\zeta^2_{(\omega)}$ (cm²/Hz)

$\omega/2\pi$ (Hz)

FIGURE   3

91

3b]. From this filtered photo we then constructed the dissipation function which is proportional to the square of the Laplacian of the surface height. A rendition of this data is shown in Figure 4. Note that the turbulence is localized onto surfaces. It is not uniformly spread out. According to these experiments the turbulent state is filled with structures or so-called "intermittency".

In order to obtain a quantitative handle on intermittency we have assigned a size to the structures according to the number of pixels that have common sides and exceed the rms power by at least a factor of 5. One now verifies that turbulent motion is characterized by large fluctuations as is shown in Figure 3a where the distribution of sizes of these structures is displayed with a dark shading. For data with randomized phases the [but same rms power] the structures are much smaller. The randomized data is displayed with a light shade. The inset to Figure 3a shows the distribution of amplitudes in a single filtered photo [solid line] as compared to the same power spectrum but with randomized phases [dashed line].

These measurements provide a quantitative basis for the development of a theory which unifies the insights that while turbulence involves a statistical description of many independent modes of fluid motion its power spectrum appears to be a finely balanced average of large fluctuations. The experimental challenges are to achieve a longer range of turbulence and resolve the time as well as spatial dependence of the structures that characterize turbulent motion.

ACKNOWLEDGMENT

REFERENCES

1. L.F. Richardson, Weather Prediction by Numerical Process, Cambridge University Press, (1922); & Proc. Roy. Soc. A110, 709, (1926)
2. L.P. Landau, E.M. Lifshitz, Fluid Mechanics (Pergamon, N.Y.) 1955.
3. Quoted in K.R. Sreenivason, Nature 344, 192 (1990).
4. W. Wright, R. Budakian, S. Putterman, Physical Review Letters, 76, 4528 (96).
5. N.B. Tufillaro, R. Ramshankar, J.P. Gollub; Order-Disorder Transition in Capillary Waves: Phys. Rev. Lett. 62,422-425, (1989).
A.B. Ezersky, S.V. Kiyashko, P.A. Matusou, M.I. Rabinovich; Domain Walls and Dislocations in Capillary Ripples: Europhys. Lett. 26,183-188 (1994).
S.T. Milne; Square Patterns and Secondary Instabilities in Driven Capillary Waves: J. Fluid Mech. 225, 81-100, (1991). B. Christianson, P. Alstrom, M. T. Levinsen; Ordered Capillary Wave States: Quasicrystals, Hexagons and Radial Waves: Phys. Rev. Lett. 68, 2157-2160 (1992).
R.Blümel,I.H. Davidson,W.P.Reinhardt,H.Lin, M.Sharnoff; Quasilinear Ridge Structures in Water Surface Waves: Phys Rev A45 ,2641-2644, (1992).
B.J. Gluckmen, P. Marq, J.Bridges, J.P. Gollub; Time-Averaging of Chaotic Spatiotemporal Wave Patterns: Phys.Rev. Lett. 71,2034-2037 (1993).
E.Bosch, W.van de Water; Spatiotemporal Intermittency in the Faraday Experiment: Phys Rev Lett: 70, 3420-3423(1993).
6. V.E. Zakharov, V.S. L'vov, G. Falkovich; Kolmogorov Spectra of Turbulence: [Springer-Berlin] 1992.

FIGURE 4

25.9
12.9
1.0

93
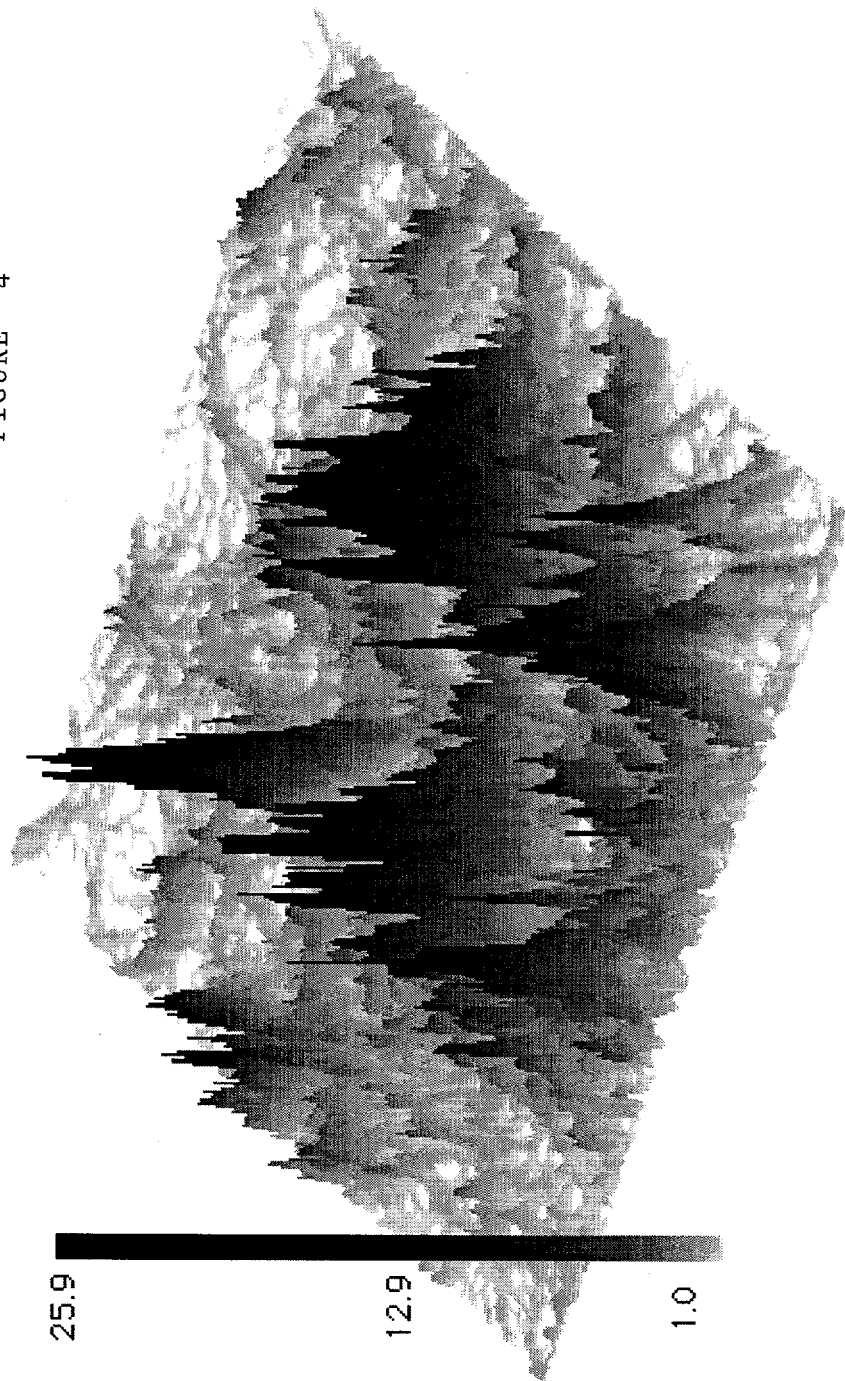
IN-FLIGHT BEHAVIOR OF DISSIMILAR CO-INJECTED PARTICLES IN THE SPRAYING OF METAL-CERAMIC FUNCTIONALLY GRADIENT MATERIALS

J.R. Fincke, W.D. Swank, and D.C. Haggard

Optical and Plasma Physics
Idaho National Engineering Laboratory
Idaho Falls, ID 83415-2211

ABSTRACT

In the spraying of functionally gradient coatings the particle ensemble delivered to the substrate can vary from a relatively low melting point metallic particle to a significantly higher melting point ceramic particle. At various stages in the spray process the particle ensemble can be either predominantly metallic, ceramic, or an intermediate combination. For co-injected particles the mixtures do not behave as a simple linear superposition of the spray patterns of the individual particle types. The particle temperature, velocity, size distributions, and pattern characteristics of the resulting spray fields is examined for all ceramic particle sprays (ZrO_2), all metallic particle sprays (NiCrAlY), and for a 1:1 mixture. The major particle-particle interaction occurs in the injector itself and results in a modified spray pattern which is different from that of either material sprayed alone. The particle velocity distributions generally exhibit a bimodal nature which is dependent on the size and density of the injected particles.

INTRODUCTION

Functionally Gradient Materials (FGMs) having either continuously or stepwise varying compositions and/or microstructures offer solutions to engineering problems involving coating systems with large differences in the coefficient of thermal expansion (CTE). A classic example where large differences in the CTEs are particularly troublesome are ceramic thermal barrier coatings (TBCs) which typically consist of the ceramic material applied over a metallic bond coat which, in turn, is applied to the surface of a metallic substrate. By continuously grading the composition of the coating from that of the bond coat material at the structure/coating interface to that of the ceramic TBC at the outer surface the stresses caused by mismatches in CTE are lessened.

One of the major objectives in the fabrication of FGMs is that the final structure should vary in a regular and consistent manner. Deviations from the planned gradient design may result in significant deviations in the properties of the gradient, such as the CTE. These deviations can then lead to localized stress concentrations and ultimately to crack formation and failure of the coating. Most of the deviations in the compositional gradient can be traced back to non-optimized spray parameters, resulting in lower than anticipated deposition efficiency. In plasma spraying low deposition efficiency for one species can often lead to banding. Banding can also occur when the trajectories of the various particle species diverge significantly between their injection into the plasma and impact on the substrate. Therefore, it is important that the inter-relationships between the particle size distributions, injection orientation, feed rates, etc., and the resulting particle trajectories and temperatures, etc., are understood.

By its nature thermal plasma spraying is well suited to the fabrication of FGMs. There exist a number of thermal spray processing methods[1,2] suitable for producing FGMs. The simplest, from a hardware, reliability, and manufacturing point of view, is the use of a single torch, fed by two computer-controlled powder feeders and a single common injector. The powders are mixed on-the-fly in a tee configuration upstream of the injector. While this configuration requires that the particle size distributions be chosen such that the particle trajectories coincide at impact the advantage of simplicity and reliability of this configuration in a manufacturing operation should not be ignored. It is also generally observed that over a wide range of operating conditions the co-injection of premixed powder generally yields a more uniform distribution of species within the graded layers[2].

This study addresses the development of an understanding the behavior of ensembles of dissimilar co-injected particles. The particle types examined are a metallic particle (NiCrAlY) and a ceramic particle (ZrO$_2$). The major particle-particle interaction occurs in the injector itself and results in a modified spray pattern which is different from that of either material sprayed alone. The spatial and statistical distributions of particle size, velocity, and temperature are also modified.

EXPERIMENTAL PROCEDURE

All testing was conducted using a Metco 9MB spray gun and two Miller model 1270 powder feeders. The powder feeders and carrier gas injection are independently computer-controlled. The spray conditions are summarized in Table 1. The powders used were a Praxair NiCrAlY, Ni-346-1, and a Sultzer-Metco stabilized zirconia, 204NS. Both powders were roughly spherical as supplied. The size distributions, obtained by sieving, appear in Figures 1 and 2. All spraying was conducted in ambient laboratory air at 86 kPa (4800 ft above sea level). A wide range of NiCrAlY:ZrO$_2$ ratios by volume were examined, however, only 1:1 by volume data will be presented in detail. In performing the spraying the feed rate of the ZrO$_2$ was held constant at 1.2 kg/hr while the feed rate of the NiCrAlY was alternately set at 1, 2, and 4 kg/hr. The two powders were also sprayed individually to provide comparison data. All particle data is acquired at an axial standoff of 100 mm.

Table 1. Thermal Spray Parameters.

Gun Type	Metco 9MB
Primary Gas	Argon (40 slm)
Secondary Gas	Hydrogen (12 slm)
Gun Voltage	75 V
Gun Amperage	600 A
Thermal Efficiency	75 %
Carrier gas	6000 sccm
	(3000 sccm each feeder for mixtures)

The experimental data acquired includes particle trajectory and pattern, particle velocity and size, and particle ensemble temperature. Particle velocity, size, and temperature statistics were also obtained and the number of cold particles estimated. Particle ensemble temperature and trajectory information consisting of the spray pattern shape, centroid position and pattern width, along with gun operating parameters and efficiency were measured by an In-flight Ltd. Torch Diagnostic System, TDS-1610, and In-flight Particle Pyrometer, IPP-2000. Particle velocity and size were measured by an Aerometrics Phase Doppler Particle Analyzer (PDPA) system. The single particle temperature diagnostic, which was designed and fabricated in-house[3,4], is integrated with the PDPA. The PDPA system does not discriminate between hot and cold particles, and only particles which generate a Doppler burst are included in the temperature statistics. This serves to tightly locate the particles spatially and by keeping track of those particles which give size and velocity information but do not yield a temperature measurement gives an estimate of the number of cold particles present. The minimum measurable particle temperature with the current experimental configuration is approximately 1300°C for 40 μm particles and somewhat higher for smaller diameter particles.
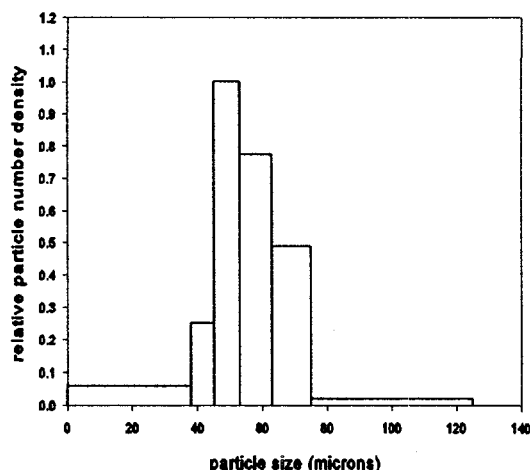
Figure 1. NiCrAlY particle size distribution obtained from sieve data.
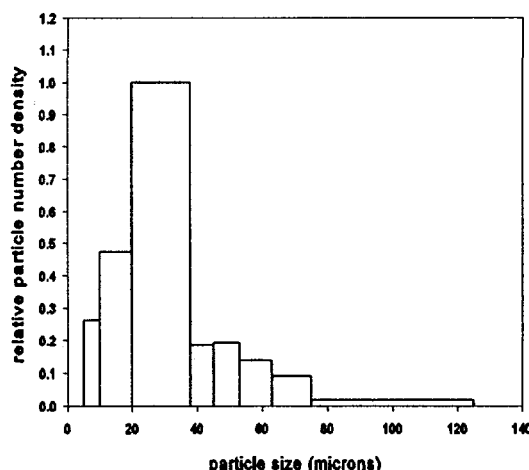
Figure 2. Zirconia particle size distribution obtained from sieve data.

RESULTS

The spray pattern shapes for the individual particle types and a 1:1 mixture (by volume) are shown in Figure 3. Also shown for reference is the sum of the two individual particle type curves. These data are obtained by imaging the light emitted by the hot particles onto the linear CCD array of a linescan camera, hence the data represent only the spatial distribution of hot particles. It is clear that the spatial distribution of the particles for the 1:1 mixture is not the simple linear super position of the individual particle types. This is because the injection velocity of the mixed system particle ensemble is different from that of either individual particle type. The average particle injection velocities and standard deviations appear in Table 2. The effect of particle-particle interactions in the close confines of the injector serves to increase the average velocity of the NiCrAlY particles while decreasing the average velocity of the ZrO_2 particles. It is interesting to note that even though the standard deviation of the injection velocity of the NiCrAlY particles is one-half that of the ZrO_2 particles the spray pattern width of the NiCrAlY powder alone is significantly broader that the zirconia only.
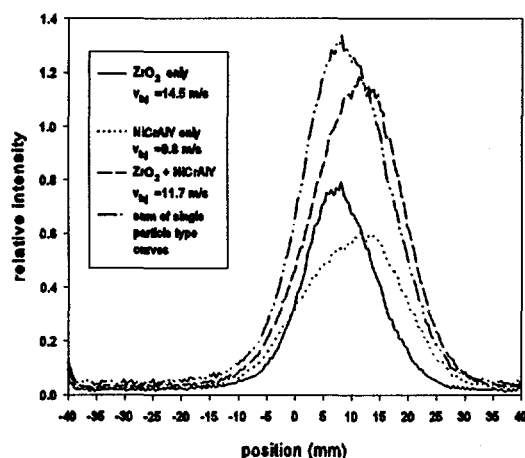
Figure 3 Spray pattern and trajectory obtained from linescan camera.

Table 2. Summary of particle injection velocities.

Particle	V_{inj} (m/s)	RMS (m/s)
ZrO_2	14.5	2.98
NiCrAlY	9.8	1.45
1:1 mix	11.7	2.40

The spatial distribution of average particle size and velocity at a standoff of 100 mm appears in Figures 4 and 5. Injection is from left-to-right. There is evidence of significant injection induced aerodynamic particle sizing, with the smallest particles being turned by the plasma jet nearer the point of injection. The larger particles with their higher momentum tend to congregate on the far side of the jet centerline. The average particle size data suggests that some aerodynamic separation of the individual particle types is also occurring, with the lighter and smaller ZrO_2 particles being preferentially closer to the point of injection and the larger, heavier NiCrAlY particles preferentially residing farther away.

The histograms of particle size on the centerline of the gun appear in Figures 6-8 for the ZrO_2, NiCrAlY, and 1:1 mix respectively. The corresponding particle velocity distributions are shown in Figures 9-11. It is interesting to note that even though the NiCrAlY particle size distribution on the centerline is much broader than that of the ZrO_2 the resulting velocity distribution is much narrower. Since there are relatively more zirconia particles than NiCrAlY particles on the centerline for the 1:1 mixture the bimodal nature of the velocity distribution is just hinted at, and the particle size distribution is skewed toward the smaller zirconia particles. The correlation between the particle velocity and particle size for the three cases is shown in Figures 12 and 13. The lighter (and smaller) zirconia particles exhibit a much stronger dependance of velocity on size than do the NiCrAlY particles.
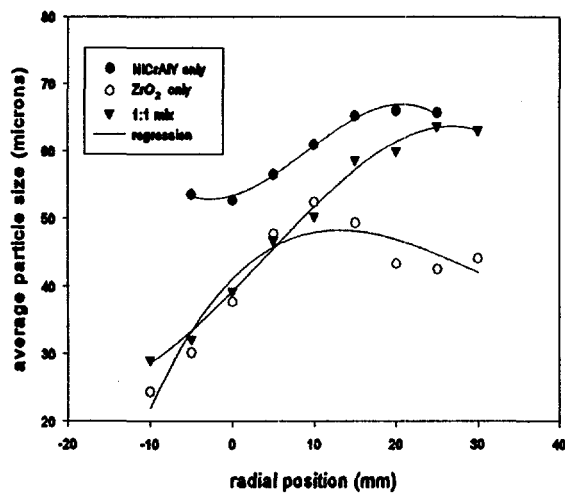
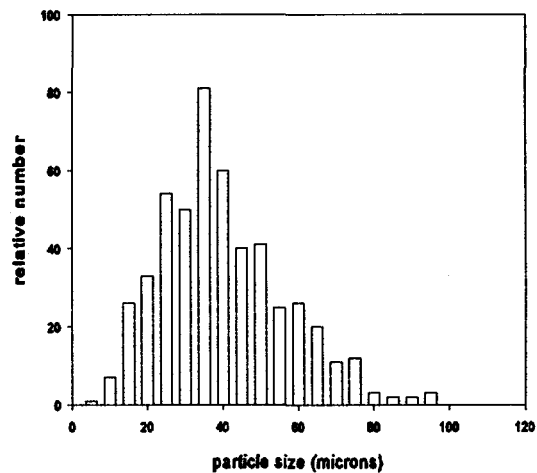**Figure 4** Radial distribution of average particle size at a standoff of 100 mm.

Figure 5 Zirconia particle size distribution on spray gun centerline.
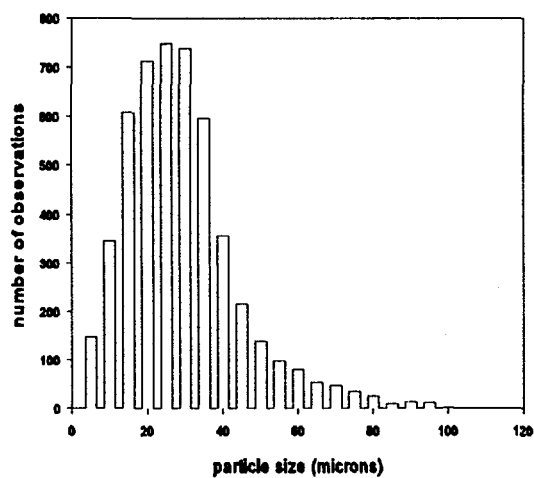

Figure 6 One-to-one by volume mixture particle size distribution on spray gun centerline.
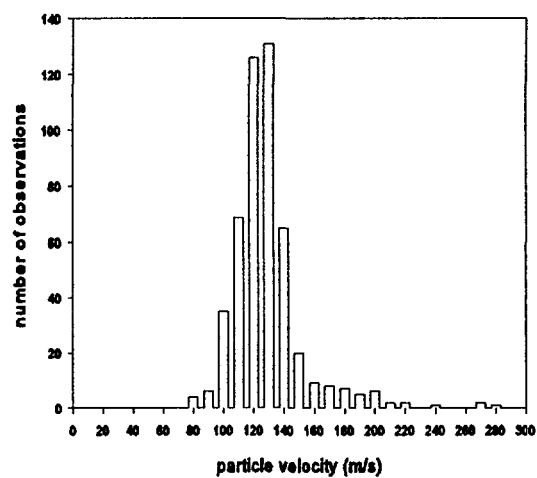

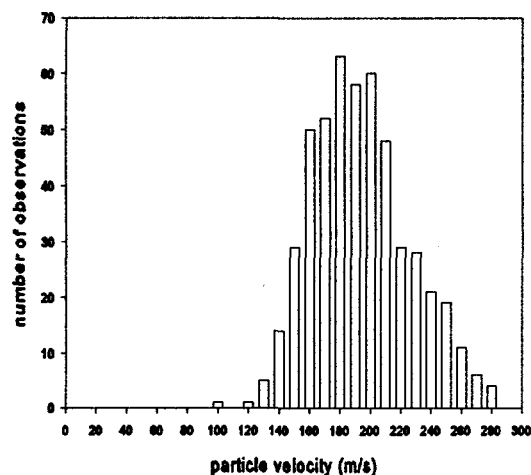**Figure 7** NiCrAlY particle velocity distribution on spray gun centerline.

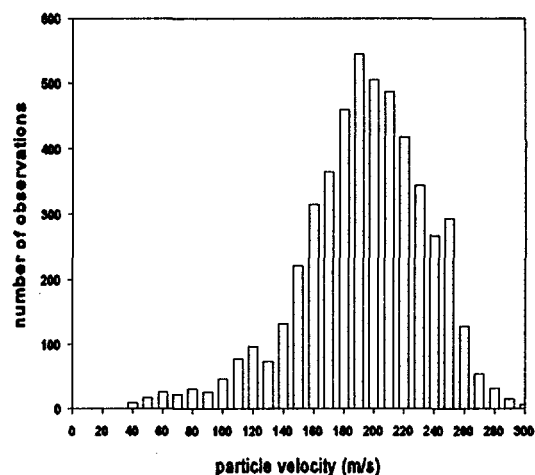**Figure 8** Zirconia particle velocity distribution on spray gun centerline.

Figure 9 One-to-one by volume mixture particle velocity distribution on spray gun centerline.
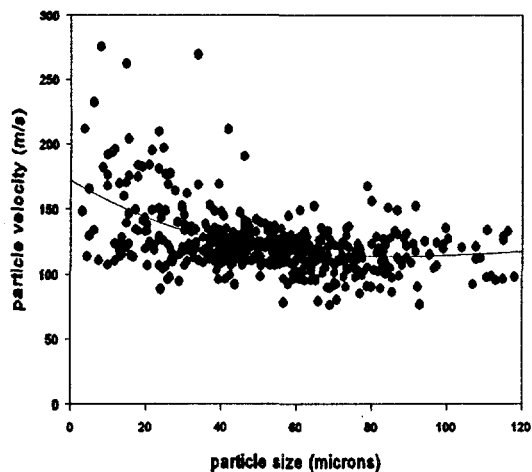

Figure 10 Correlation between particle velocity and diameter for zirconia NiCrAlY, centerline measurement.
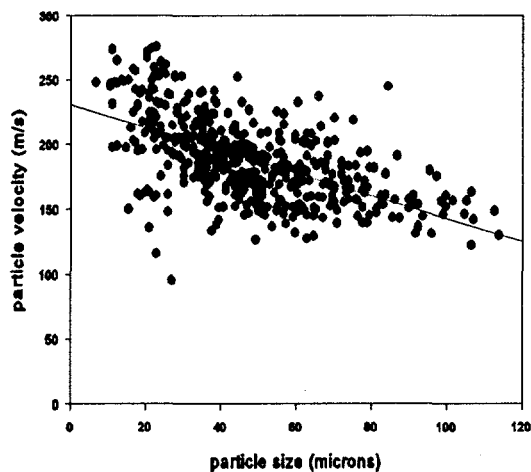

Figure 11 Correlation between particle velocity and diameter for zirconia powder, centerline measurement.

For the 1:1 mixture, (Figure not shown), the range of observed particle velocities is increased with the denser NiCrAlY particles exhibiting lower velocities. The histograms of particle temperature on the gun centerline appear in Figures 14-16. The average NiCrAlY particle temperature is well above the melting point of (~1500 °C) and is significantly lower than the mean temperature of the zirconia particles which is very near their melting point of 2620 °C. The temperature distribution for the 1:1 mixture is very similar to that for the zirconia due to their relatively larger number. The data indicate that approximately 65% of the NiCrAlY particles observed were

99

hot, that is, yield a measurement of temperature, while approximately 50% of the zirconia particles were hot. Of the hot NiCrAlY particles >95% were above the melting temperature, while only approximately 50% of the zirconia particle observed were greater than the melting temperature. Near the maximum particle concentration (spray pattern center) at approximately -15mm, there are roughly equal numbers of NiCrAlY and zirconia particles. Under these conditions the bimodal nature of the velocity distribution becomes more apparent, Figure 17, and the particle size and temperature distributions broaden, Figure 18 and 19. The broadening of the temperature distribution, which is strongly dependent on the size distribution is accompanied by a decrease in the number of hot particles, to less that 35% with the fraction that are molten being even less.
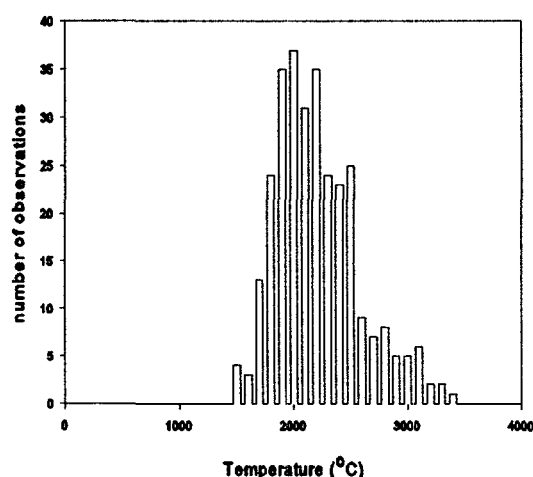

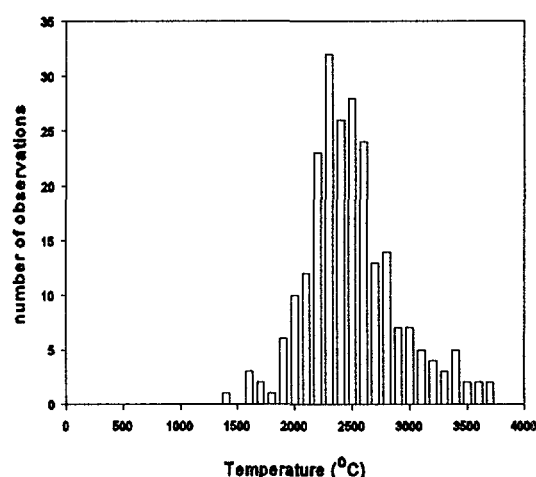**Figure 12** NiCrAlY particle temperature distribution on spray gun centerline.

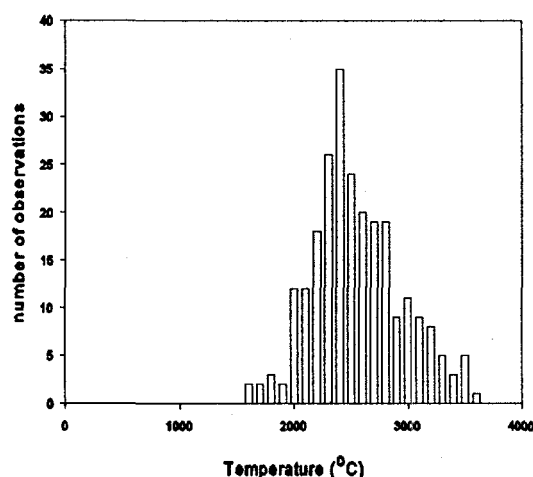**Figure 13** Zirconia particle temperature distribution on spray gun centerline.

Figure 14 One-to-one by volume mixture particle temperature distribution on spray gun centerline.
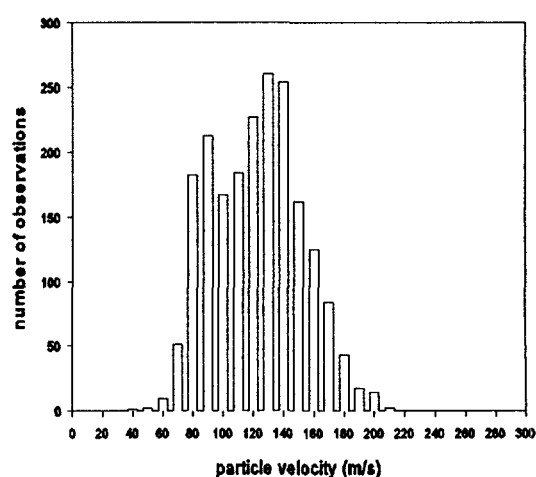

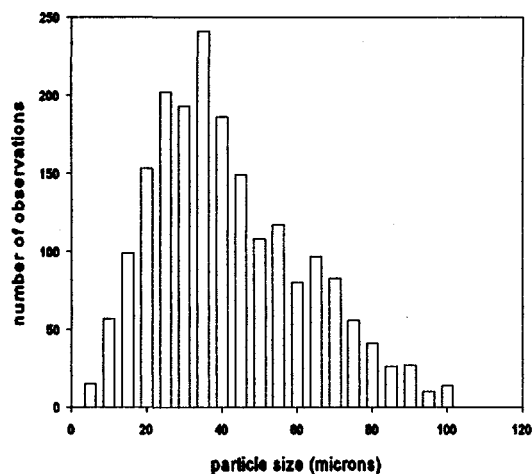**Figure 15** One-to-one by volume mixture particle velocity distribution at spray pattern center.

100

Figure 16 One-to-one by volume mixture particle size distribution at spray pattern center.
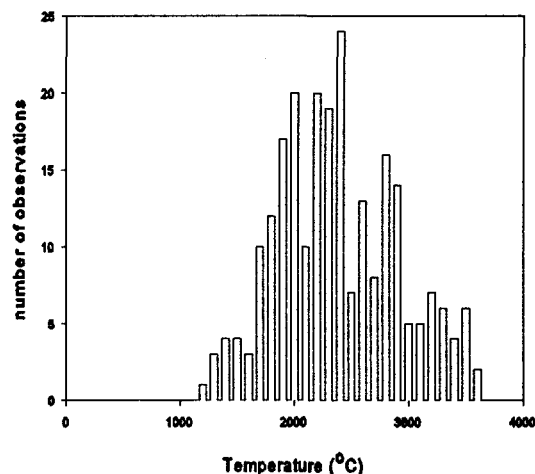
Figure 17 One-to-one by volume mixture particle temperature distribution at spray pattern center.

CONCLUSIONS

The co-injection of dissimilar particle types is complicated and significantly influenced by particle-particle interactions in the close confines of the injector. Because of this, the resulting spray field is more complicated than a simple linear superposition of individually injected single particle types. On the gun centerline approximately 65% of the metallic particles are estimated to be above the melting point, while only about 25% of the zirconia particles are above their melting point. Near the spray pattern center for 1:1 mixtures, less than 35% of the particles are "hot" and even fewer are at or above their respective melting points. In designing spray schedules for the fabrication of FGMs, the fact that deposition efficiency is influenced by spray trajectory, which in turn is influenced by mixture ratios and particle-particle interaction in the injector, must be considered and accounted for.

ACKNOWLEDGMENTS

REFERENCES

1. Sampath, S., Herman, H, Shimoda, N., and Saito, T., MRS Bulletin, **20** (1995) 27.
2. Smith, W., Jewett, S., Sampath, S., Berndt, C., Herman, H., Fincke, J., and Wright, R., Thermal Spray: Practical Solutions for Engineering Problems, ASM international, (1996) 317.
3. Fincke, J., Swank, W., Jeffery, C., IEEE Transactions on Plasma Science, **18** (1990) 948.
4. Fincke, J., Swank, W., Jeffery, C., and Mancuso, C., Measurement Science Technology, **4** (1993) 559.

HELICAL WAVES AND NON-LINEAR DYNAMICS OF FLUID/STRUCTURE INTERACTIONS IN A TUBE ROW

F.C. Moon, M. Thothadri

Cornell University
Ithaca, New York 14853, U.S.A.

Abstract

The goal of this study has been to investigate low-dimensional models for fluid-structure dynamics of flow across a row of cylindrical tubes. Four principle results of this experimental-theoretical study are discussed. i) Experimental evidence has shown that the dynamic instability of the tube row is a subcritical Hopf bifurcation. ii) The critical flow velocity decreases as the number of flexible cylinders increases. iii) The linear model exhibits coupled helical wave solutions in the tube dynamics. iv) A nonlinear model of the tube motions shows a complex subcritical Hopf bifurcation with a secondary bifurcation to a torus or quasi-periodic oscillation. In this analysis the tools of center manifolds, normal forms and numerical simulation are used.

INTRODUCTION

It is well known that fluid-elastic instabilities and vibrations are responsible for numerous failures in heat exchange systems in the power industry. Linear models in fluid-structure dynamics are well known (e.g., Chen (1978)). However only recently have nonlinear models and analysis been used to explore the post-flutter dynamics. Our focus in this study is the cross flow of air across a row of flexible cylinders.

Connors (1970) studied the instability in a row of circular cylinders, measured the quasi-static forces and put forth a simple empirical criterion for the critical flow velocity. Research over the past couple of decades has been concentrated on predicting this critical flow velocity for different configurations. Approximate empirical results exist for certain array configurations, but no general result applicable to all configurations has been found.

The lack of understanding of the actual mechanics of the fluid-structure interaction has prevented most attempts from predicting fluid forces in sufficient detail. A few attempts have been made to get at the basis of these fluid forces, Paidoussis & Price (1988) , Chen (1978), Leaver & Weaver (1982). Although a very good insight has been obtained through these studies, their inability to predict the structural dynamics for a general system has led numerous studies to experimentally determine the fluid forces, Tanaka & Takahara (1981), Chen *et al.* (1993).

Paidoussis (1987) provides a review of the work in fluid-elastic instabilities due to internal flow, external axial flow, annular flow and cross-flow. A similar review on fluid-elastic instabilities due to cross-flow is provided by Weaver *et al.* (1987), Chen (1989).

Some nonlinear models have been put forth to capture the global behavior of the structure, Bishop and Hassan (1964), Hartlen and Currie (1970), Price *et al.* (1990). The most popular one being the Hartlen-Currie model or the wake-oscillator model. The chaotic dynamics due to impacting of the cylinders with their supports have been studied by some researchers recently; Chen *et al.* (1993). Paidoussis has reported that a rotated array on cross-flow loses stability in a supercritical Hopf bifurcation. Muntean (1995) at Cornell reported that a single cylinder in a row of rigid tubes loses stability by a negative damping mechanism in a sub-critical Hopf bifurcation and put forth a nonlinear model capturing some of the characteristics.

DESCRIPTION OF EXPERIMENTS

The wind tunnel in this study is a standard blower type low turbulence air tunnel. The test section is 91.5 cm long and is made of plexiglass. Figure 1 shows an isometric view of the test section. The test section is 256 mm × 256 mm in cross-section. The row of cylinders is positioned about 30.5 cm downstream from the upstream end of the test section. The cylinder row, consisting of nine cylinders, has seven oscillating cylinders and a fixed cylinder at each end.

Each oscillating cylinder has two degrees-of-freedom, displacements inline and transverse to the flow. Each of the oscillating cylinders is made of a hollow plexiglass tube, 19 mm OD – 16 mm ID, 256 mm long and has a mass per unit length of 0.23 kg/m. Fixed cylinders at the ends are solid 19 mm OD rods of Aluminum and are bolted to the structure containing the cylinders, thus holding the entire structure in place. A 91.5 cm long, 1.6 mm diameter steel rod passes through the cylinder caps and support their gravity. These steel rods are pinned at the top and the bottom ends, providing the cylinders with the required degrees of freedom. The pitch-to-diameter ratio is 1.35. The relative static position of the cylinders in the inline direction can be adjusted by increasing or decreasing the length of the springs, keeping all the cylinders aligned. The natural frequency of the cylinders in the inline direction is 7.4 Hz and 6.8 Hz in the transverse direction. The damping ratio in still air was found to be close to 0.013 in both directions.

Figure 2 shows evidence for a *subcritical Hopf bifurcation*. This bifurcation diagram for the *central cylinder* is obtained with all the seven cylinders oscillating, i.e. the responses of only the central cylinder were used to obtain Figure 2. The bifurcation diagram for the rest of the cylinders seemed to be qualitatively similar to the one found for the central cylinder. For small flow velocities, the cylinder oscillations were small amplitude turbulent buffetting due pressure fluctuations, flow noises, etc. The amplitude of these oscillations are found to increase almost linearly with flow velocity as has been reported in earlier studies, Muntean (1995), Blevins (1977). Moreover, as the flow velocity is increased, the stochastic component of the cylinder response decreases. No modal patterns of oscillations could be detected in the cylinder row for turbulent buffetting.

As the flow velocity is increased further, small scale buffeting of the cylinders persists, but *sufficiently* large perturbations of the cylinders result in large amplitude, periodic limit

cycle oscillations. The frequency of these limit cycle oscillations was found not to vary much with flow velocity. The reduced flow velocity at the sub-critical Hopf bifurcation was found to be, $U_{cr} \approx 115$. Beyond this critical flow velocity only large amplitude oscillations are present and further increase in the flow velocity leads to impacting of the cylinders with the support structure. To estimate the amplitude of the unstable limit cycle the central cylinder was perturbed from the buffetting oscillations by giving it a known displacement in the direction of the flow (initial velocity is zero). The smallest such displacement that resulted in the large amplitude limit cycle oscillations (upper branch) was recorded as the amplitude of the unstable limit cycle for the corresponding flow velocity.

The variation in the critical reduced flow velocity as the number of oscillating cylinders was found. This experiment was performed by allowing a certain number of cylinders to oscillate while restraining the motions of the rest. The number of cylinders of cylinders was increased in a symmetric fashion around the central cylinder. As the number of oscillating cylinders is increased, the *critical flow velocity* was found to *decrease*. The onset of instability for a single oscillating cylinder was far removed from those for more than one cylinder. Thus coupling between the cylinders drastically reduces the onset of instability.

THEORETICAL MODEL

The equations of motion of nth the cylinder, with respect to a frame fixed at its equilibrium position, is given by

$$M \left\{ \begin{array}{c} \ddot{x}_n \\ \ddot{y}_n \end{array} \right\} + \left[\begin{array}{cc} C_x & 0 \\ 0 & C_y \end{array} \right] \left\{ \begin{array}{c} \dot{x}_n \\ \dot{y}_n \end{array} \right\} + \left[\begin{array}{cc} K_x & 0 \\ 0 & K_y \end{array} \right] \left\{ \begin{array}{c} x_n \\ y_n \end{array} \right\} = \boldsymbol{f}_n \tag{1}$$

where the terms on the left-hand side are the inertial, damping and stiffness terms of the cylinder structure and $\boldsymbol{f}_n$ on the right-hand side is a vector containing the fluid forces on the nth tube in the x and y directions. The displacements of the nth cylinder are denoted by x_n and y_n.

The profile of the flow (upstream) across the cylinder row was experimentally found to be fairly uniform and the cylinders are coupled only by the fluid flowing past them, i.e. there is no structural coupling.

As a result of the uniformity of the flow across the cylinder row and the periodicity of the cylinders, any set of three cylinders has a symmetry along the flow direction about the middle cylinder. The fluid force on the nth cylinder due to the relative motions of the (n−1)th and the (n+1)th cylinder are related by $\boldsymbol{f}_n^{n-1} = \boldsymbol{f}_n^{n+1}$ for the direct coupling of the x and y directions and by $\boldsymbol{f}_n^{n-1} = -\boldsymbol{f}_n^{n+1}$ for the cross coupling between the x and y directions. Using these symmetry conditions and linearizing the fluid forces about the cylinder equilibrium positions we have,

$$\begin{aligned}
\boldsymbol{f}_n = & -\tfrac{1}{2}\rho D U \left(\left[\begin{array}{cc} \alpha' & -\sigma' \\ -\tau' & \beta' \end{array} \right] \left\{ \begin{array}{c} \dot{x}_n - \dot{x}_{n-1} \\ \dot{y}_n - \dot{y}_{n-1} \end{array} \right\} + \left[\begin{array}{cc} \alpha' & \sigma' \\ \tau' & \beta' \end{array} \right] \left\{ \begin{array}{c} \dot{x}_n - \dot{x}_{n+1} \\ \dot{y}_n - \dot{y}_{n+1} \end{array} \right\} \right) \\
& + \rho U^2 \left(\left[\begin{array}{cc} \alpha'' & -\sigma'' \\ -\tau'' & \beta'' \end{array} \right] \left\{ \begin{array}{c} x_n - x_{n-1} \\ y_n - y_{n-1} \end{array} \right\} + \left[\begin{array}{cc} \alpha'' & \sigma'' \\ \tau'' & \beta'' \end{array} \right] \left\{ \begin{array}{c} x_n - x_{n+1} \\ y_n - y_{n+1} \end{array} \right\} \right)
\end{aligned} \tag{2}$$

The single-primed quantities, $(\alpha\,',\sigma\,',\beta\,',\tau\,')$ are the fluid-damping coefficients and the double-primed quantities, $(\alpha\,'',\sigma\,'',\beta\,'',\tau\,'')$ are the fluid-stiffness coefficients. The notation used here is slightly different from the one used by Chen *et al.* (1993b).

The coefficients $\alpha\,''$, $\alpha\,'$ couple the x-motions of adjacent cylinders and $\beta\,''$, $\beta\,'$ couple y-motions. The coefficients $\tau\,''$, $\sigma\,''$, $\tau\,'$, $\sigma\,'$ couple the x (y)-motions of one cylinder to the y (x)-motions of the adjacent cylinders. The direct coupling coefficients were measured by using the ARMA process (Auto Regressive Moving Average) and the cross coupling coefficients were determined through heuristic fits based on instability mechanisms.

ANALYTICAL RESULTS

We consider a traveling wave solution to Equations 1 and 2 of the form

$$\left\{ \begin{array}{c} x_n \\ y_n \end{array} \right\} = \left\{ \begin{array}{c} a_1 \\ a_2 \end{array} \right\} e^{i(qn-\omega t)} \tag{3}$$

where, $q = 2\pi\kappa P$; κ is the wave number (i.e. $\frac{2\pi P}{q}$ is the wave length), ω is the angular frequency and P (pitch) is the periodicity associated with the structure. In the above traveling wave solution, the $e^{-i\omega t}$ characterizes the temporal behavior of the solution for the initial data given by e^{iqn}. The quantity q, is the phase difference between adjacent cylinders and hence characterizes the spatial distribution of the cylinders at any instant of time.

The traveling wave solution, Equation 3, written compactly as $\boldsymbol{x} = \boldsymbol{a}e^{i(qn-\omega t)}$, implies that $\boldsymbol{x}_{n+1} = \boldsymbol{x}_n e^{iq}$. This implies that the frequency $\omega(q)$ has a period 2π in q, i.e. $\omega(q) = \omega(q+2\pi)$ and as $q = 2\pi\kappa P$, the above periodicity leads to $q(\kappa) = q(\kappa + \frac{1}{P})$. If we restrict q between $[-\pi,\pi]$ then $-\frac{1}{2P} \le \kappa \le \frac{1}{2P}$ which means the wavelength $\lambda \ge 2P$.

If q is complex the real part of q contributes to the spatial distribution of cylinders (wave patterns) and the imaginary part results in *spatial* growth or decay(depending on the sign) as $n \to \infty$ at any given time. These waves with complex wave numbers are called *evanescent waves* or *cutoff waves*.

Figure 3 shows a helical wave mode for $u_r = 90$.

By this representation, the wave in Figure 3 *at any instant in time*, is a helix that circles around the $+x$-axis in the counter-clockwise direction. The points of constant phase advance in the $+x$-direction with velocity, ω_r/q_1. Moreover, any cylinder (i.e. for a fixed n) will circle the $+x$-axis in the clockwise direction for this wave.

For the fixed-ends boundary condition (i.e. $\boldsymbol{x}_o = \boldsymbol{x}_{N+1} = 0$), the constraint of zero displacements for the end cylinders implies that the wave numbers q, can no longer be purely real. The imaginary part of the wave numbers are positive and this ensures that the waves are spatially decayed to satisfy the boundary conditions at the ends for all time.

NONLINEAR BIFURCATION ANALYSIS

Our ultimate goal is to understand what the nature of the nonlinear forces are that lead to a subcritical dynamic instaiblity. These instabilities are very dangerous in practice. The subcritical phenomenon however depends on the nonlinear nature of the fluid coupling forces. In the absence of dynamic measurements of the nonlinear part of the fluid forces, we posit a plausible nonlinear model. In this model we consider two tubes; one constrained to

vibrate transverse to the flow, and the other constrained to vibrate in the flow direction. We represent the dynamics of this sytem by the equations;

$$
\left\{ \begin{array}{c} \dot{x} \\ \dot{y} \\ \ddot{x} \\ \ddot{y} \end{array} \right\} = \boldsymbol{A}(u_r) \left\{ \begin{array}{c} x \\ y \\ \dot{x} \\ \dot{y} \end{array} \right\} + \left(\frac{u_r}{u_{cr}} \right)^2 \left\{ \begin{array}{c} 0 \\ 0 \\ C_{30}\dot{x}^3 + C_{31}\dot{x}^2\dot{y} + C_{32}\dot{x}\dot{y}^2 + C_{33}\dot{y}^3 \\ D_{30}\dot{y}^3 + D_{31}\dot{y}^2\dot{x} + D_{32}\dot{y}\dot{x}^2 + D_{33}\dot{x}^3 \end{array} \right\} + \frac{u_r}{u_{cr}} \left\{ \begin{array}{c} 0 \\ 0 \\ C_{50}\dot{x}^5 \\ D_{50}\dot{y}^5 \end{array} \right\}
$$

$$(4)$$

where, $\boldsymbol{A}(u_r) = \left[\begin{array}{cc} \boldsymbol{O} & \boldsymbol{I} \\ -\boldsymbol{K}(u_r) & -\boldsymbol{C}(u_r) \end{array} \right]$

is the matrix governing the linearized equations, $\boldsymbol{K}$ is the non-symmetric stiffness matrix, $\boldsymbol{C}$ is the damping matrix and u_r is the parameter in the system, the reduced flow velocity. The various elements of the stiffness and damping matrices were obtained for the two degree-of-freedom system from the linear model obtained earlier.

In this model u_r represents a normalized flow velocity, while u_{cr} is the critical flow velocity for flutter when two of the eigenvalues of A cross the imaginary axis.

The *center manifold theorem* ensures that for the full nonlinear equations there exists a subspace (center manifold) which is tangential to the subspace spanned by the eigenvectors, at the equilibrium point. The flow close to the equilibrium point approaches the center manifold asymptotically. The theorem also ensures that the stability of the equilibrium point in the full nonlinear equations is the same as the stability when restricted to flow on the center manifold. Moreover, any additional equilibrium point or limit cycles which occur in a neighborhood of the given equilibrium point on the center maifold are gauranteed to exist in the full nonlinear equations.

Near-identity transformations of increasing order were used to reduce the flow on the center manifold, obtained from the center manifold analysis described above, to a normal (canonical) form. After reducing the equations to a normal form a further transformation into polar coordinates was carried out (see Rand and Armbruster (1987)).

The system of Equation 4 was studied through numerical simulation. The amplitude of the limit cycles in the Bifurcation diagram was obtained by using Newton's root finding method on the Poincare Map, obtained by taking a Poincare section at $\dot{y} = 0$. The stability of the limit cycles were obtained from the eigenvalues of the Jacobian evaluated at the limit cycle. See Figures 4 and 5.

Figure 4 shows the subcritical branch of the unstable limit cycle that occurs at the critical flow velocity predicted by linear theory. At lower flow velocities both a stable limit cycle of large amplitude is shown as well as a torus on quasi-periodic vibration (characterized by two incommensurate frequencies). These results were obtained by using a Poincare map technique shown in Figure 5, which plots $\{x,\ y,\ \dot{x}\}$ when $\dot{y} = 0$. A point or dot indicates a limit cycle or periodic oscillation, while a closed curve indicates a quasi-periodic oscillation.

CONCLUSIONS

This study has shown that experimental dynamic instabilities in tubes in cross flow can exhibit subcritical limit cycle oscillations (Hopf bifurcation). These subcritical Hopf bifurcations are dangerous in practice because large amplitude oscillations can be induced at

much lower flow velocities than those predicted by classical linear models for fluid-structure instability. The nature of these subcritical instabilities depends on the nonlinear fluid and structural forces. We have used an ad-hoc nonlinear model to show the possible complexities in the secondary bifurcations as a function of flow velocity. This study has demonstrated the need to obtain better measurements of dynamic fluid structure forces in order to provide realistic predictive models of nonlinear fluid-structure instabilities.

REFERENCES

1. R.D. BISHOP and A.Y. HASSAN, "The lift and drag forces on a circular cylinder in flowering field". In *Proceedings of the Royal Society of London, Series A, 277*, pages 51–75, (1964).

2. R.D. BLEVINS, *Flow-Induced Vibrations*. Van Nostrand Reinhold Company, (1977).

3. S.S. CHEN, "Crossflow-Induced Vibrations of Heat Exchanger Tube Banks," *Nuclear Engineering and Design*, 47:67–86, (1978).

4. S.S. CHEN, S. ZHU, and J.A. JENDRZEJCZYK, "Motion-dependent Fluid Forces Acting on Tube Arrays in Crossflow," Research Report ANL-93/15, Argonne National Laboratory, (1993).

5. H. CONNORS, Jr., "Fluid-elastic Vibration of Tube Arrays Excited by Cross Flow," in D.D. Reiff, editor, *Flow-Induced Vibration in Heat Exchangers*, pages 42–56. ASME, (1970).

6. J.H. LEAVER and D.S. WEAVER, "A Theoretical Model for Fluid-elastic Instability in Heat Exchangers," *ASME Journal of Pressure Vessel Technology*, 104:147–158, (1982).

7. G. MUNTEAN, *Influence of Fluid Wake Structure on the Dynamics of a Flexible Tube Row in Cross Flow*, Ph.D. Thesis, Cornell University, (1995).

8. M.P. PAIDOUSSIS, "Flow Induced Instabilities of Cylindrical Structures," *Applied Mechanics Review*, 40(2):163–175, (1987).

9. M.P. PAIDOUSSIS and F.C. MOON, "Nonlinear and Chaotic Fluid-Elastic Vibration of a Flexible Pipe Conveying Fluid," *Journal of Fluids and Structures*, 2:567–591, (1988).

10. M.P. PAIDOUSSIS and S.J. PRICE, "The Mechanisms Underlying Flow-induced Instabilities of Cylinder Arrays in Cross Flow, *Journal of Fluid Mechanics*, 187:45–59, (1988).

11. R.H. RAND, and D. ARMBRUSTER, *Perturbation Methods, Bifurcation Theory and Computer Algebra*, Springer-Verlag, (1987).

12. H. TANAKA and S. TAKAHARA, "Fluid-elastic Vibration of tube Array in Cross Flow," *Journal of Sound and Vibration*, 77(1):19–37, (1981).

13. D.S. WEAVER And J.A. FITZPATRICK, "A Review of Flow Induced Vibrations in Heat Exchangers," In *Proceedings of the International Conference in Flow-Induced Vibrations*, pages 1–17, (1987).
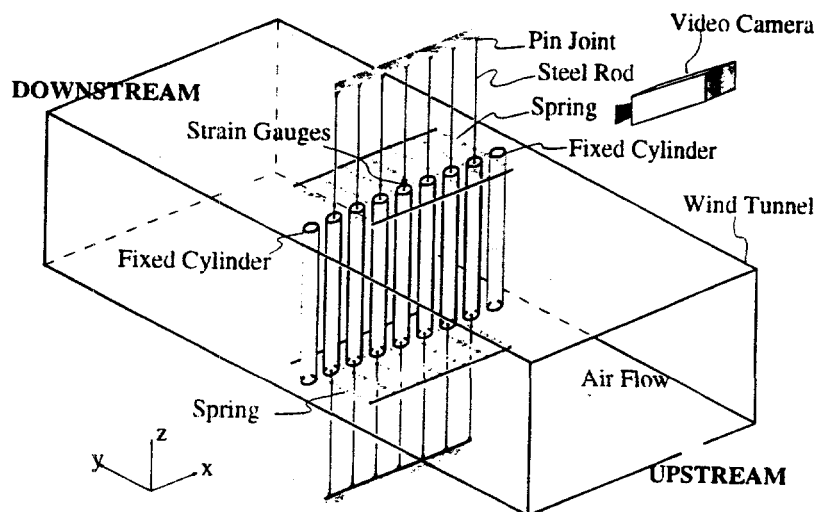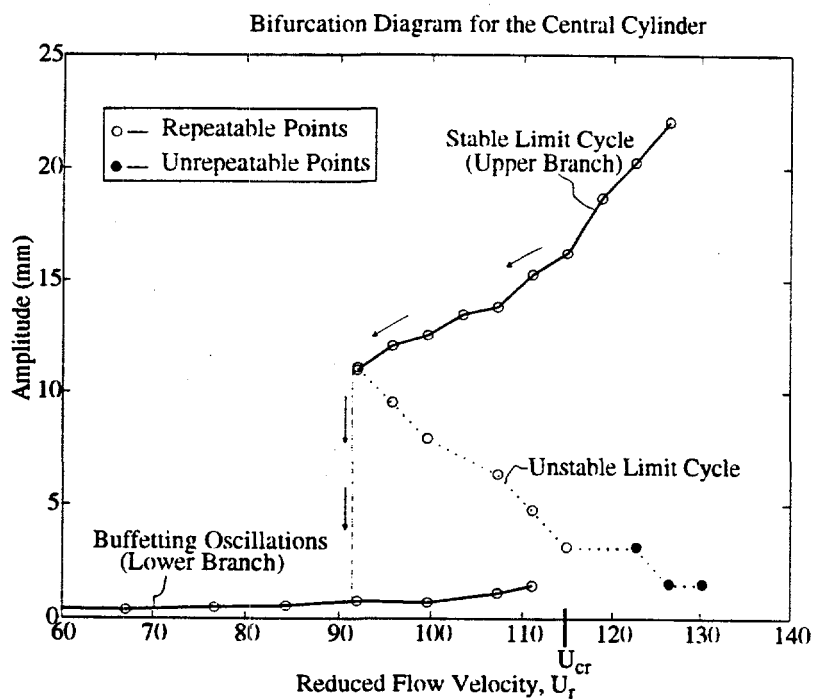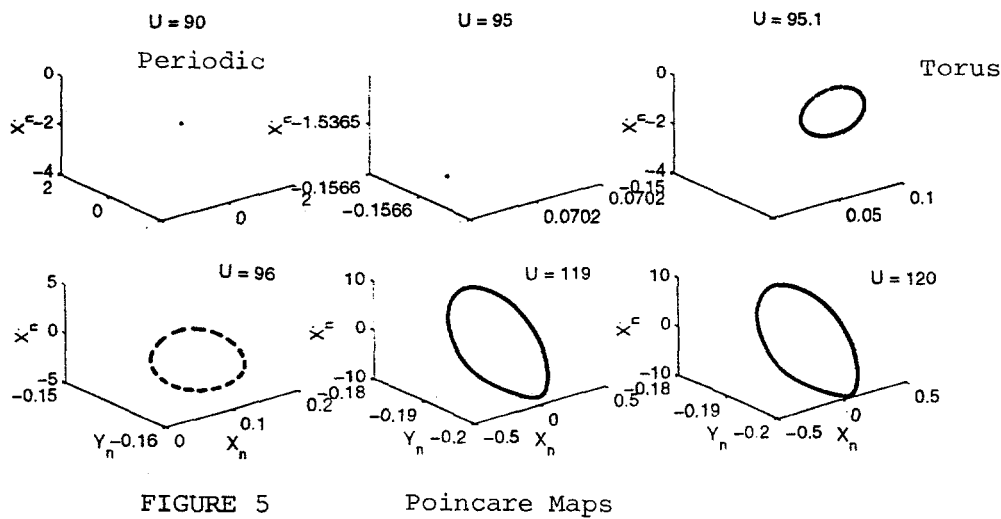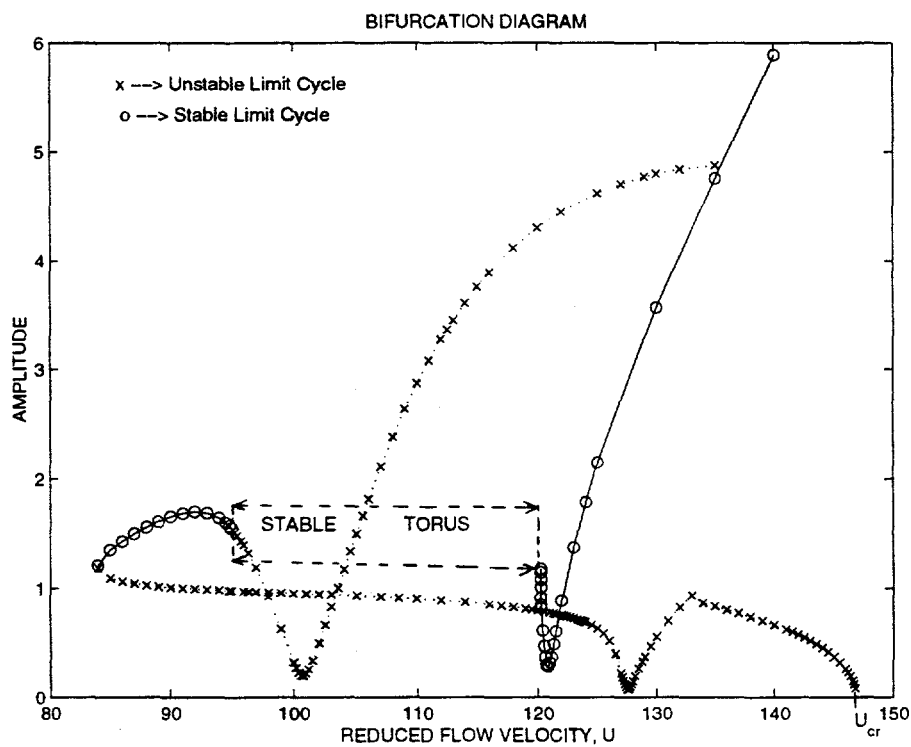
FIGURE 1

Bifurcation Diagram for the Central Cylinder

FIGURE 2

108

$U_r = 90$

Helical Wave Mode

FIGURE 3

BIFURCATION DIAGRAM

x ---> Unstable Limit Cycle
o ---> Stable Limit Cycle

STABLE   TORUS

AMPLITUDE

REDUCED FLOW VELOCITY, U

U_{cr}

FIGURE 4

U = 90   U = 95   U = 95.1

Periodic   Torus

U = 96   U = 119   U = 120

FIGURE 5   Poincare Maps
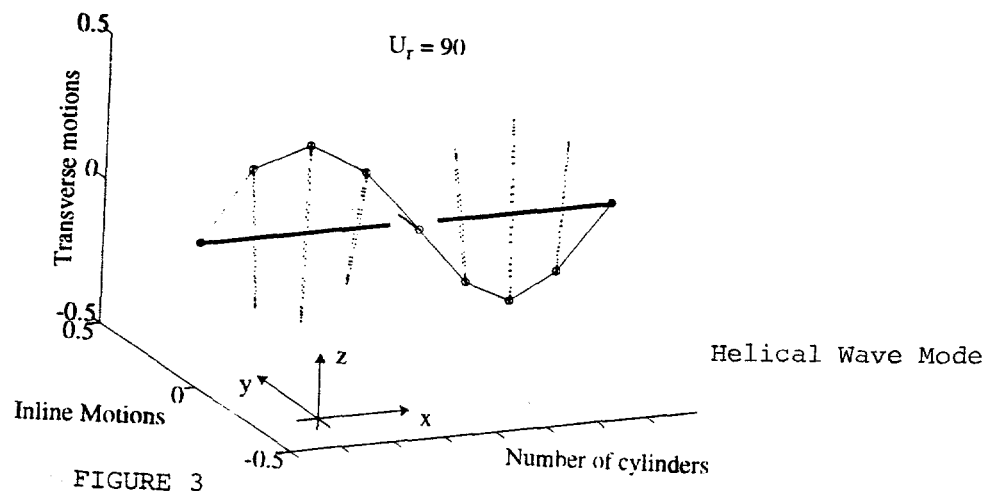
FUNDAMENTAL STUDIES OF SPRAY COMBUSTION

S.C. Li, P.A. Libby and F.A. Williams

Center for Energy and Combustion Research
and
Department of Applied Mechanics and Engineering Sciences
University of California, San Diego
La Jolla, CA 92093-0411

ABSTRACT

Our research on spray combustion involves both experiment and theory and addresses the characteristics of individual droplets and of sprays in a variety of flows: laminar and turbulent, opposed and impinging. Currently our focus concerns water and fuel sprays in two stage laminar flames, i.e., flames arising, for example from a stream of fuel and oxidizer flowing opposite to an air stream carrying a water spray. Our interest in these flames is motivated by the goals of reducing pollutant emissions and extending the range of stable spray combustion. There remains considerable research to be carried out in order to achieve these goals. Thus far our research on the characteristics of sprays in turbulent flows has been limited to nonreacting jets impinging on a plate but this work will be extended to opposed flows with and without a flame. In the following we discuss details of these studies and our plans for future work.
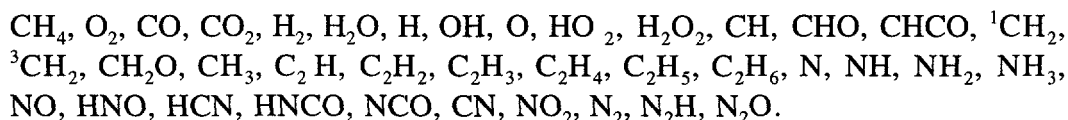
WATER SPRAYS IN TWO STAGE LAMINAR FLAMES

To improve understanding of the chemical and fluid mechanical interactions between water droplets and the formation of NOx in flames we have carried out studies of two stage laminar flames. To do so we have employed our counterflowing burner which is the principal device used in our experimental effort. In these studies one stream is a fuel-rich mixture of methane and air with a stoichiometric ratio denoted Φ while the opposed stream involves air and a spray consisting of relatively small water droplets. Different droplet loadings and different flow conditions permit us to investigate the influence of strain rates and water concentration on NOx formation in flames.

110

Under the conditions we have studied there exists a vaporization plane, i.e., a plane close to the flame by which all the water has vaporized. Because of the relatively low temperature of the gas mixture at this plane, the distribution of temperature in the flame is altered by the water which therefore has both a chemical and a thermal influence.

In these flames there occur a green premixed reaction zone in which the oxidizer in the methane-air stream is consumed, a blue diffusion zone in which the residual fuel components namely CO and HO are consumed by the air in the air-droplet stream and finally a vaporization plane as noted earlier. In the neighborhood of the axis all three of these surfaces are flat and parallel to one another. The separation distance between them decreases with increasing rates of strain and equivalence ratio of the fuel-air stream. In experiments on these flames temperature profiles are measured with thermocouples and concentration profiles of the stable species are measured by gas chromatography.

Complementing in an important way these experiments are theoretical-numerical studies in which relatively complete descriptions of the fluid mechanics and chemistry of these flows from the exit plane of one jet to the exit plane of the other are considered. The present computations involve 140 elementary reactions among the following 38 species:

CH_4, O_2, CO, CO_2, H_2, H_2O, H, OH, O, HO_2, H_2O_2, CH, CHO, $CHCO$, $^1CH_2$, $^3CH_2$, CH_2O, CH_3, C_2H, C_2H_2, C_2H_3, C_2H_4, C_2H_5, C_2H_6, N, NH, NH_2, NH_3, NO, HNO, HCN, $HNCO$, NCO, CN, NO_2, N_2, N_2H, N_2O.

Both experiment and computation show that the methane and oxygen in a fuel rich mixture react rapidly in the premixed zone to form CO and H whose concentrations reach maxima as the methane disappears. The further oxidation of CO and H to form CO and HO occurs in the diffusion zone. The C_2 species such as C_2H_2, C_2H_4 and C_2H_6 are predicted to be produced rapidly in the early stages of the premixed zone but these species are consumed in the diffusion zone. The concentrations of the C_2 species strongly depend on the stoichiometry of the methane-air mixture; the larger the value of Φ the higher the concentrations of these species, a finding consistent with the observed soot emissions in fuel rich methane-sir flames. Water is the most important agent for the consumption of the radical CH which leads to prompt NOx. Thus the addition of water to flames not only reduces prompt NOx because of its reduction of CH but reduces thermal NO_x because of its reduction of the maximum temperature. This dual effect has been widely known but our study has established the rate of the crucial reaction $CH + H_2O \rightarrow CH_2O + H$.

Figures 1 and 2 present some of the results of our studies. These figures show the distributions across the flame of the temperature and mole fraction of NO for various fuel-air ratios. Figures 1 and 2 relate to these flames without water and with 10% water addition respectively. The important result shown here is that there is a 50% reduction in peak NO concentration with water addition. Further results are given in Fig. 3 where the emission index E is plotted versus equivalence ratio for various rates of water addition. Again we see the significant benefit realized from the addition of water.
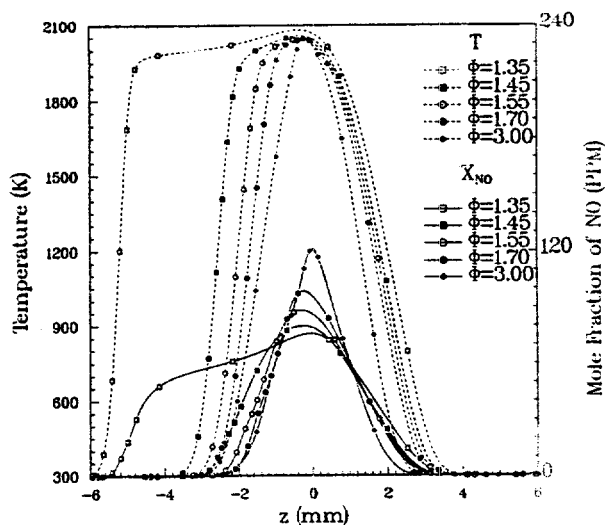
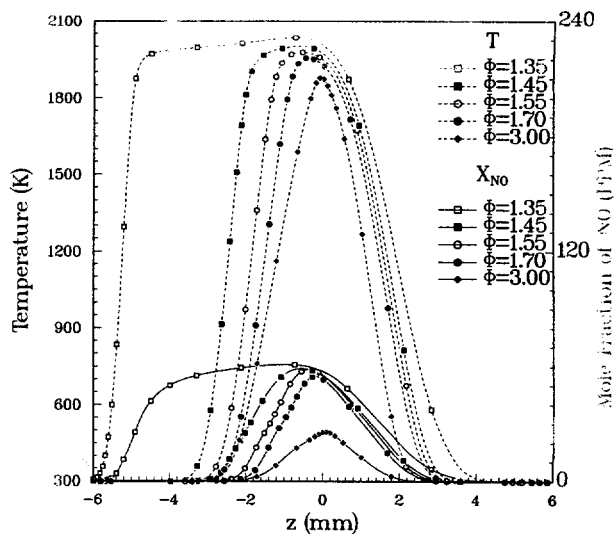Figure 1.   Computed profiles of temperature and NO concentration without water.

Figure 2.   Computed profiles of temperature and NO concentration with 10% water added in air stream.
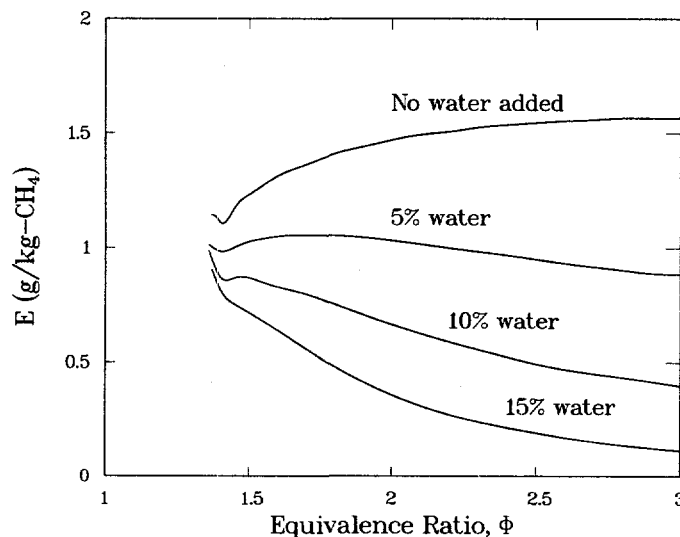

Figure 3. Predicted NO emission index as a funciton of equivalence ratio and mass percentage of water added to the air stream

TWO-STAGE METHANOL SPRAY FLAMES

In earlier studies reported in [1, 2] we have described the combustion of fuel droplets carried in a nitrogen stream counter to an air stream. This configuration results in the usual spray diffusion flame but we have recently been studying two-phase, two-stage flames which are analogous to those discussed in the previous section but with water replaced by fuel. We thus consider fuel droplets carried by air flowing counter to an airstream. The droplet loading is such

112

that the fuel-air stream is fuel rich, i.e., has a value of Φ greater than unity. Such flames have several distinct advantages in particular that they permit the chemistry of fuel sprays under a wide rage of reaction zone conditions to be studied both experimentally and computationally. In particular coordinated studies of these flames permit the identification of the reactions which are critical to the combustion of liquid fuels in much that same fashion as we were able to identify the critical reactions for the chemical inhibition of NOx formation by water. Moreover in experiments the increased thickness of the reaction zone results in improved spatial resolution and thus increased data accuracy.

Our recent research on two phase methanol flames has involved a stream of droplets transported in air with an equivalence ratio ranging from 1.6 to 3.0 and a fuel side rate of strain varying from 50 s^{-1} to 100 s^{-1}. The droplet sizes are such that again there is a vaporization plane. Moreover the flame also involves a pale green premixed zone and a blue diffusion zone. The same experimental techniques as described earlier are employed to measure the distributions of temperature and concentrations of the stable species and the same computational methods described earlier are brought to bear. Here comparison of experiment and computation permit values of several key reaction rates of uncertain value to be determined.

The distribution along the axis of the computed axial velocity for a typical flow is shown in Fig. 4. We have data only for the portion of the flow in which droplets exist but for that limited region excellent agreement is seen. Also shown are the experimental data on the Sauter mean diameter; the rapid decrease in droplet diameter in the neighborhood of the edge of the flame is consistent with the existence of a vaporization plane as noted earlier. The interesting increase in the mean diameter upstream of that plane is a consequence of the larger diameters being decelerated to a lesser extent than the smaller droplets in the decelerating gas stream. In due course even these larger droplets are vaporized.
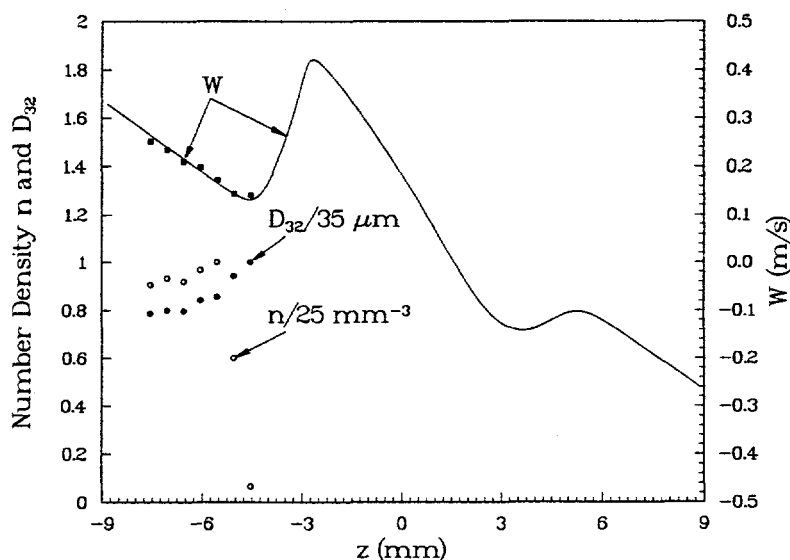

Figure 4. Profiles of axial velocity, number density and Sauter mean diameter on the burner axis.

In Fig. 5 we compare computed and measured distributions of the temperature and major species. We see two high temperature regions corresponding to the two reaction zones discussed earlier, namely the diffusion zone at z = 2 mm and the lower temperature premixed zone at z = 3 mm. Comparison of Figs. 4 and 5 establishes that the peaks in the velocities coincide with the temperature maxima. The experimental and computed distributions of the concentrations of various species shown in Fig. 5 are in excellent agreement. Of particular interest is the location of the peaks in the CO and H_2 concentrations implying agreement as to the location of the premixed zone.
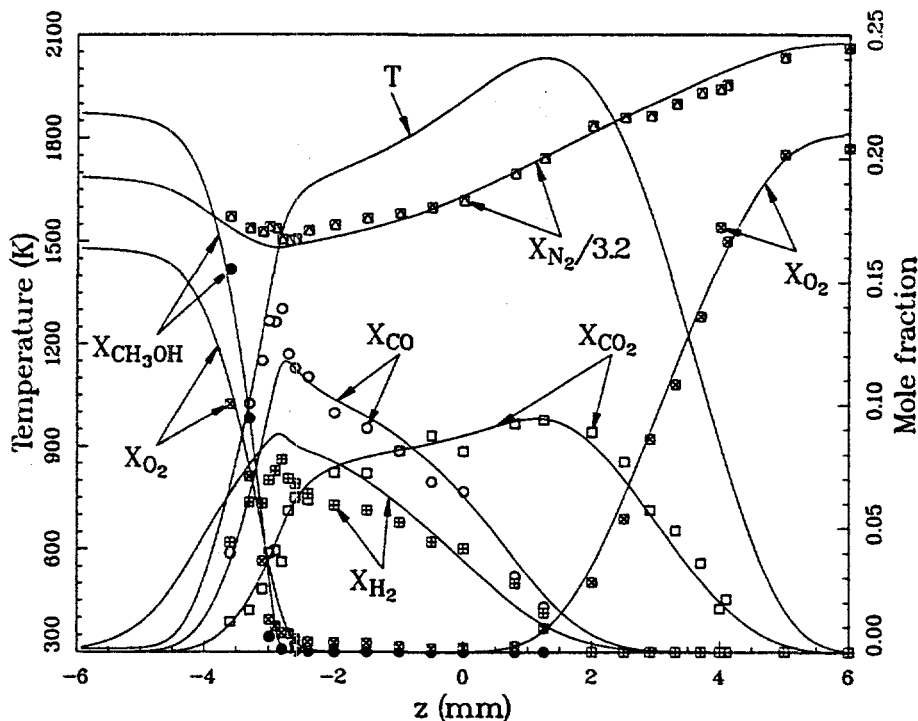

Figure 5. Comparison between measurement and prediction of profiles of temperature and concentration for $\Phi = 2$ with $a = 50$ s^{-1}.

In Fig. 6 we show the experimental and computed distributions of the mole fraction of the various C_2 species, namely C_2H_2, C_2H_4 and C_2H_6. Two sets of computed results are shown; for the solid curves the chemistry is the same as that used in Fig. 5 while for the dashed curve the isomerization reaction $CH_3O + M \rightarrow CH_2OH + M$ has been removed. This removal is seen in Fig. 6 to displace the premixed zone appreciably toward the stagnation plane and to increase the peak concentrations of methane and the C_2 species. This influence of one crucial reaction demonstrates the value of coordinated experimental and computational studies in establishing the correct chemistry in these systems. Because of its significantly greater concentration of the OH radical, this figure also demonstrates the importance of H atoms in these flames. By comparing experiment and computation we are able to deduce a rate constant for the reaction $CH_2OH + H \rightarrow CH_3 + OH$ which is the dominant reaction in the formation of CH_4 and C_2 species. Previous values for this constant were found to be in error.
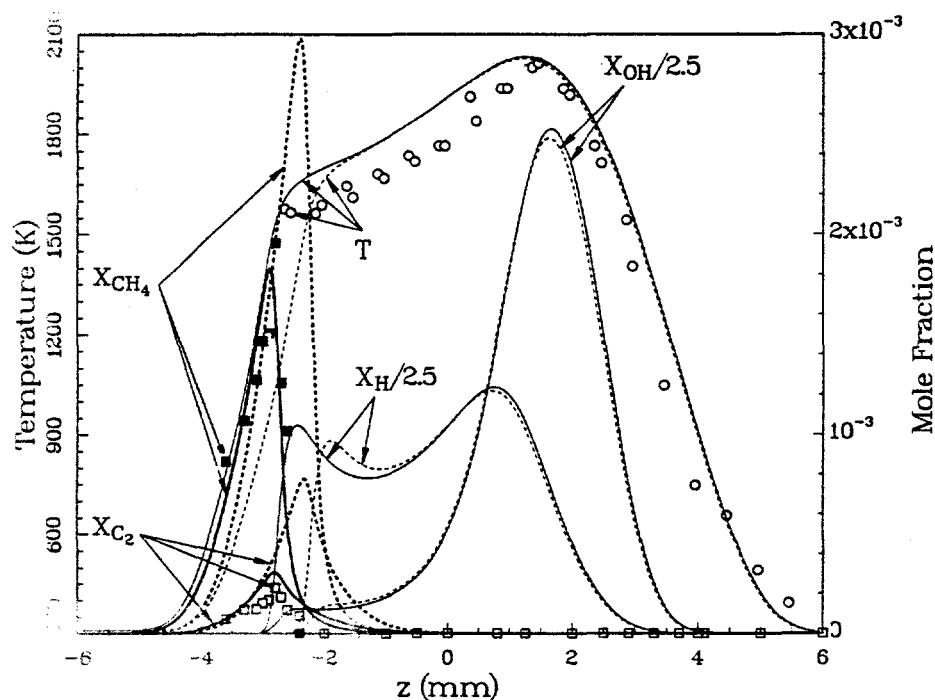
114

Figure 6. Comparison between measurement and prediction of profiles of temperature and concentrations of minor species for $\Phi = 2$ with $a = 50$ s^{-1}.

TURBULENT SPRAYS IN STAGNATION FLOWS

Our studies of turbulent sprays have involved a stream impinging on a wall. In this case a grid is installed near the exit plane of the jet. We again use our PDPA to measure two velocity components and droplet diameter. Our spray generator is operated so as to produce a relatively wide range of droplet diameters such that for our flow conditions the smallest droplets can be considered to follow the fluctuations in gas velocity. We are thus able to obtain at various positions in the flow the statistics of the velocity of the gas and of droplets of various sizes. A more direct measurement of relative velocities would involve simultaneous measurements of gas and droplet velocities at a particular point in space and time. This is beyond the capability of our current instrumentation but in the near future a particle image velocimetry system will be brought to bear on this problem.

Despite this limitation we have used our data to construct a simplified description of the response of droplets of different sizes to turbulence. A feature of this description is that two bounding droplet sizes can be estimated: The largest droplets that effective respond to turbulent

velocity fluctuations and the smallest droplets that are immune to such fluctuations. Figure 7 presents these results for our experiment in which the Kolmogorov wave number is estimated to be 185 and the wave number corresponding to the integral scale is three; plotted are the droplet diameter in microns against the normalized wave number of the velocity fluctuations. Thus for a given wave number we obtain the two diameters in question. The theory reported in Fig. 7 can be used to make similar plots for other turbulent flows, i.e., those with different spectral ranges.
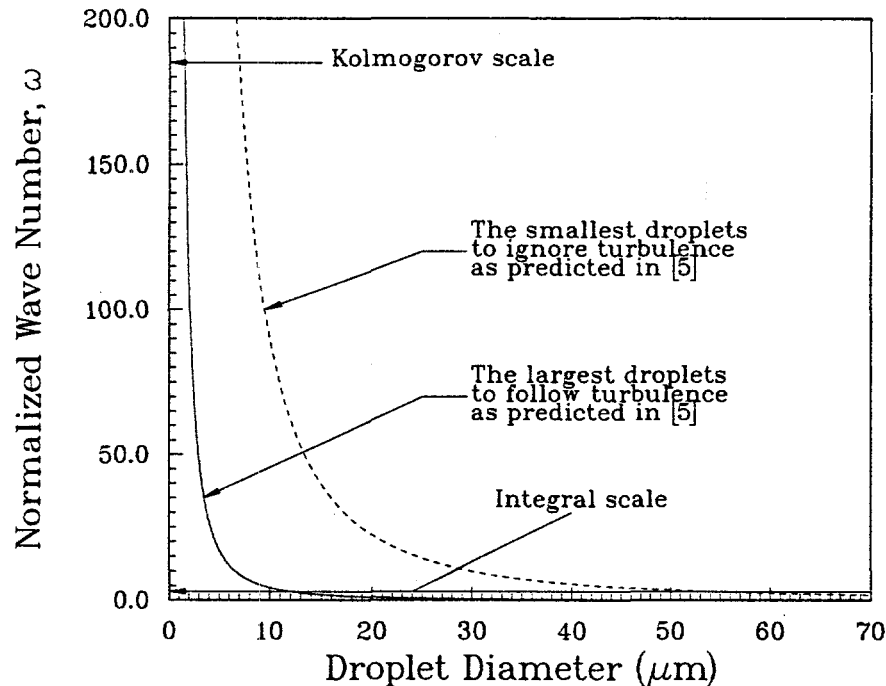

Figure 7. The largest droplets to follow and smallest droplet to ignore turbulent fluctuations of various scales.

LAMINAR COUNTERFLOWING STREAMS IN A NARROW CHANNEL

In one of our earlier investigations we studied the dynamics of droplets in non-reactive opposed laminar flows [1]. Of particular interest in the present context was the finding that for a given set of flow conditions, i.e., jet spacing and jet velocities, droplets of a well defined range of sizes would oscillate across the stagnation plane. Provided a drag law is assumed the dynamics of such droplets are readily studied since the flow field is simply and accurately described. However, there is an essential experimental difficulty of photographing the motion of such droplets in axisymmetric jet flows, namely that the droplets always leave the focal plane of the camera and are lost for purposes of observation. The remedy we found was to photograph the response of the droplets in an opposed slot flow. In this case opposed flows enter the passage between two plates and leave in orthogonal directions. The resultant flow has three planes of symmetry. While this configuration permitted the oscillations in question to be readily photographed, the flow field in

116

which the droplets move must be analyzed if calculated and observed droplet trajectories are to be compared. As a consequence we have been studying the flow field in question.

From a fundamental point of view this slot flow is an addition to the various relatively simple fundamental solutions to the Navier-Stokes equations and is therefore of interest on its own. By invoking the various symmetry requirements and restricting attention to narrow slots we obtain a set of three partial differential equations with two independent variables: the streamwise coordinate and the coordinate normal to the walls. The dependent variables are the streamwise velocity, the transverse gradient of the transverse velocity and the pressure. Not surprisingly a single parameter appears in these equations, namely a Reynolds number. As is typically the case in fundamental flows, solutions to these equations are readily obtained for two limiting cased, i.e., for small and large Reynolds numbers. For intermediate values numerical solutions involving iteration must be constructed.

At the present time the numerical analysis of the limiting cases is completed and examples for intermediate Reynolds numbers are being considered. When the analysis of the flow field in these slots is completed, comparison of the observed and photographed trajectories will be undertaken.

REFERENCES

1. S.C. LI, "Spray Stagnation Flames," invited review paper by *Progress in Energy and Combustion Science* (accepted), (1997).

2. S.C. LI, P.A. LIBBY and F.A. WILLIAMS, "Spray Impingement on a Hot Surface in Reacting Stagnation Flows," *AIAA J.* 33, 1046 (1995).

3. S.C. LI, N. ILINCIC and F.A. WILLIAMS, "Reduction of NO_x Formation by Water sprays in Strained Two-Stage Flames," ASME paper No. 96-GT-545, presented at ASME Turbo-Expo '96, Birmingham, England UK, June 10-13, 1996 and accepted for publication in *ASME Journal of Engineering for Gas Turbines and Power* (accepted) (1996). Also *ASME* No. 96-GT-545.

4. S.C. LI, and F.A. WILLIAMS, "Experimental and Numerical Studies of Two-Stage Methanol Flames," *Twenty-Sixth Symposium (International) on Combustion*, The Combustion Institute, Pittsburgh, PA, pp. 1017-1024 (1997).

5. S.C. LI, P.A. LIBBY and F.A. WILLIAMS, "Turbulent Sprays in Stagnation Flows," *Atom. Sprays* 5, 287 (1995).

FILM COOLING IN A PULSATING STREAM

H. Fasel, A. Ortega, I. J. Wygnanski
Department of Aerospace and Mechanical Engineering,
The University of Arizona,
Tucson AZ 85721
USA

ABSTRACT

The mean flow and stability characteristics of a plane, laminar wall jet were investigated experimentally, theoretically, and numerically for a constant wall temperature boundary condition. The streamwise mean velocity and temperature profiles and the downstream development of the hydrodynamic and thermal boundary layer thicknesses were obtained through simultaneous hot and cold wire measurements. Even at relatively low temperature differences, heating or cooling of the surface sufficiently altered the mean velocity profile in the inner region to produce significant effects on the jet stability. Selective forcing of the flow at the most amplified frequencies produced profound effects on the velocity and temperature fields and hence the time-averaged shear stress and heat transfer. Large amplitude excitation of the flow at high frequencies resulted in a **reduction** in the maximum skin friction by as much as 65% with an **increase** in the maximum wall heat flux as high as 45%. The skin friction and wall heat flux were much less susceptible to low frequency excitation.[*]

NOMENCLATURE

Re_j	Reynolds number measured at exit plane $= \rho U_j d / \mu$	Y_m	maximum normal distance from the wall (for the integration domain), m
T	local mean temperature, K	c_p	specific heat of air at free-stream, J/kg-K
T_o	free-stream temperature, K	d	wall jet slot width, m
T_w	wall temperature, K	k	thermal conductivity, W/m-K
U	local streamwise mean velocity, m/s	$\dot{m}$	mass flow rate, kg/s
U_j	jet exit velocity, m/s	t'	fluctuating temperature, K
U_m	local maximum streamwise velocity, m/s	u'	fluctuating streamwise velocity, m/s
U_o	free-stream velocity, m/s	x,y	coordinates, m

Greek symbols

δ denotes boundary layer thickness, m

δ_v local hydrodynamic boundary layer thickness, m

δ_t local thermal boundary layer thickness, m

μ free-stream dynamic viscosity, N-s/m^2

ρ free-stream density, kg/m^3

Subscripts

j jet exit plane

m maximum

o free-stream

t thermal

v hydrodynamic

w wall

INTRODUCTION

The wall jet is a thin jet of fluid introduced tangentially along a surface. The free-stream can either be co-flowing or quiescent. This flow field consists of two primary unstable shear layers that are associated with two different kinds of instability modes: a viscous (inner) mode associated with the inner near-wall region, and an inviscid (outer) mode associated with the inflection point in the outer region. Wall jets have important technological applications such as in de-icing or de-fogging of windshields. In film cooling of gas turbine components, a turbulent wall jet is used to shield blades and other surfaces exposed to high temperature freestream flow. In previous explorations of the wall jet, Katz et al. (1992) and Zhou et al. (1993) found that among other effects, significant reductions in average skin friction can be obtained in a turbulent wall jet by excitation of the flow at its dominant mode. Given the importance of the wall jet in the transport of heat and mass to or from surfaces, it is important to question whether forcing may have similar related effects on the convective heat transfer. The possibility of augmenting or reducing the wall heat transfer, with minimal energy expenditure for excitation, would lead to innovative methods for controlling heat transfer. The wall jet thus provides a fundamental yet practical flow for investigating the possibility of enhancing or suppressing rates of transport by both active and passive flow control.

Theoretical investigations of the incompressible, isothermal, laminar wall jet were first performed by Tetervin (1948) and Glauert (1956) who obtained a closed form solution. Results were substantiated by the hot wire measurements of Bajura and Szewezyk (1970). Cohen et al. (1992) theoretically investigated the effects of blowing and suction on an incompressible laminar wall jet. They found a new family of self-similar solutions in which Glauert's solution is a member. These self-similar solutions were later confirmed experimentally by Amitay & Cohen (1993). The self-similar solutions of the temperature field for a low speed, laminar, incompressible wall jet with constant physical properties were obtained by Schwarz & Caswell (1961) for the special cases of constant wall temperature, varying wall temperature, and constant wall heat flux. Mitachi & Ishiguro (1974) performed a theoretical investigation of the laminar wall jet with different wall thermal boundary conditions. The linear stability of the wall jet was investigated by Chun & Schwarz (1967), Bajura & Szewezyk (1970), Bajura & Catalano (1975), and Mele et al. (1986). They showed that the initial stages of transition are two-dimensional in nature, and are dominated by the mechanism of vortex pairing, which is commonly observed in free shear flows.

We present recent experimental and numerical results to show the effects of low and high excitation levels on the velocity and temperature fields of a two-dimensional, laminar wall jet flowing over a constant temperature surface. Experiments and numerical computations were performed for a steady, unforced wall jet followed by a wall jet with low amplitude forcing. Surprisingly, it was found that under most circumstances, forcing decreased the time-averaged wall shear stress while the wall heat transfer was increased.

DESCRIPTION OF EXPERIMENTS

The experiments were performed in a thermally controlled, closed return, low speed, air wind tunnel as shown in Fig. 1. The test section was 711 mm wide, 165 mm high and 2,362 mm long. A slot type wall jet

apparatus was used which essentially duplicates the design of Zhou et al. (1993) which was used in the study of a turbulent wall jet with forcing. This apparatus consisted of a 0.5 HP centrifugal blower, acoustic muffler, air-water heat exchanger, diffuser, a plenum chamber fitted with an acoustic speaker, three screens of 30, 40 and 50 mesh size and a contraction nozzle having a variable area ratio. In these experiments the area ratio was 28:1 resulting in a jet slot width of 3.2 mm and a jet exit velocity of 1.5 m/s. The apparatus was designed to fit in the test section floor of an existing closed return wind tunnel which will provide the free-stream flow in future experiments. The flow exited the wall jet apparatus tangentially over an isothermal heat transfer surface. The surface consisted of a 19 mm thick highly polished aluminum tooling plate which was held at constant temperature by means of cooled/heated water from a recirculating chiller that counter flowed through milled slots inside the plate. Surface temperatures were measured with Type K thermocouples that were potted into the surface with an aluminum epoxy. The measurements of the streamwise velocity and temperature were conducted using two side-by-side (7 mm apart) standard Disa Model 55P11 single hot and cold wire probes with a 5 μm diameter tungsten sensor having length-to-diameter ratio of 300. The hot wire was kept at an over-heat ratio of 1.6 and had a maximum frequency response of 30 kHz. The frequency response of the cold wire was 600 Hz. The cold wire was calibrated against a NIST traceable lab standard thermistor probe. The external forcing was introduced using acoustic perturbations produced by a 12 inch speaker cone that was placed in the diffuser of the wall jet apparatus shown. A digital-to-analog converter was used to generate the forcing signal which was passed through an amplifier before it was used to activate the speaker. The forcing frequencies were determined from linear stability theory, and the excitation level measured at the jet exit plane was incrementally varied from 0.6 to 2.0 %. In this investigation the forcing frequencies were fixed at 43.9 Hz and 21.1 Hz corresponding to the inner and outer modes of instability. In order to retain phase information, the phased locked technique was used in which the hot wire, the cold wire and the function generator records, consisting of 256 points each, were digitized simultaneously and saved. At each measuring point, up to 800 events were recorded.
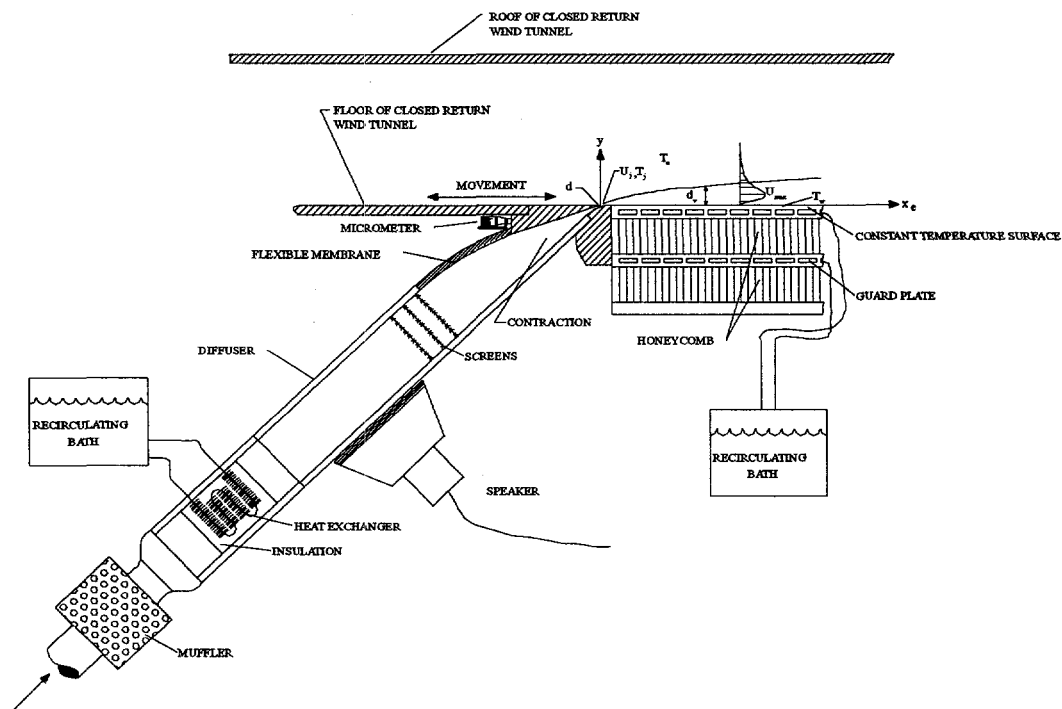

Figure 1: The experiment apparatus.

EXPERIMENTAL RESULTS

Undisturbed Mean Flow

Three sets of experiments were conducted corresponding to three temperature ratios denoted by T_w/T_o: wall cooling with $T_w/T_o = 0.98$, wall heating with $T_w/T_o = 1.03$ and the neutral case with $T_w/T_o = 1$, in which the surface, jet exit, and free-stream temperatures were all the same. Throughout the experiments, the jet exit Reynolds number, $Re_j = \rho U_j d/\mu$, remained fixed at 320. The normalized mean profiles of the streamwise velocity measured for the three cases above and at three normalized streamwise locations ($x/d = 12$, 16, and 20) are shown in Fig. 2. The local maximum velocity, U_m, and the local thickness of the hydrodynamic boundary layer, δ_v (where the mean velocity is equal to $U_m/2$ in the outer region), were used to render all variables dimensionless. Figure 2a shows full velocity profiles for all cases, while Figs. 2b, 2c, and 2d present the inner region in more detail for the cooling, neutral, and heating cases, respectively. The symbols represent the experiments while the solid line corresponds to Glauert's (1956) theoretical prediction. The agreement between the experiments and the theory for the neutral case is good except in the inner region where the velocity gradient of the experimental data is higher, Fig. 2c. This may be due to the relatively high turbulence level (0.5%) of the jet. When cooling is applied, Fig. 2b, the inner velocity gradient increases and the maximum velocity is shifted closer to the surface. Heating the surface, Fig. 2d, appears to have the opposite effect, but the differences in the heated case compared to the neutral case cannot be claimed to be outside of the range of experimental uncertainty. Despite these small changes in the mean velocity due to heating and cooling, a more significant effect is observed on the fluctuating streamwise velocity distribution.

Mean Flow Field Subjected to External Forcing

The mean velocity and temperature fields were next investigated under conditions with externally applied forcing. Disturbances were introduced into the flow at various frequencies and amplitudes. Three cases, corresponding to the above three values of T_w/T_o, were studied. In this section only the results for the heating case are presented. The dimensional mean profiles of the streamwise velocity measured for the heating case and at three normalized streamwise locations ($x/d = 12$, 16, and 20) are shown in Fig 3. Figure 3a presents the case in which the flow is excited with a high frequency disturbance (approximately 44Hz for inner mode forcing), while Fig 3b corresponds to a low frequency disturbance (21Hz for outer mode forcing.) The excitation level is defined at $x/d = 0$ as $100 \cdot u'_m/U_j$, where, u'_m is the maximum fluctuating streamwise velocity (measured by using the phase-locked data technique) and U_j is the jet mean exit velocity. As is shown in Fig 3a, when inner mode forcing is applied the velocity field is dramatically altered. The effects become more pronounced as the downstream distance increases. The effect of outer mode forcing is not as dramatic because the growth rates associated with the outer mode are smaller than the inner mode growth rates, as predicted by the theory (see Amitay & Cohen (1996)). In order to see the effects of forcing on the wall shear stress, the near wall region of the velocity field was plotted and is presented in Fig 4. Seven cases, corresponding to the unforced case, inner and outer mode forcing with 0.6%, 1% and 2% excitation levels, are presented. Figures 4a, 4b and 4c represent the experimental data taken at $x/d = 12$, 16, and 20, respectively. The solid line corresponds to the velocity gradient for the unforced case. For low levels of excitation, the velocity gradient near the wall is negligibly affected. As the excitation level is increased to 2% the velocity gradient near the wall is decreased by up to 15% (with respect to the unforced case) for the outer mode forcing, and by up to 65% for the inner mode forcing.
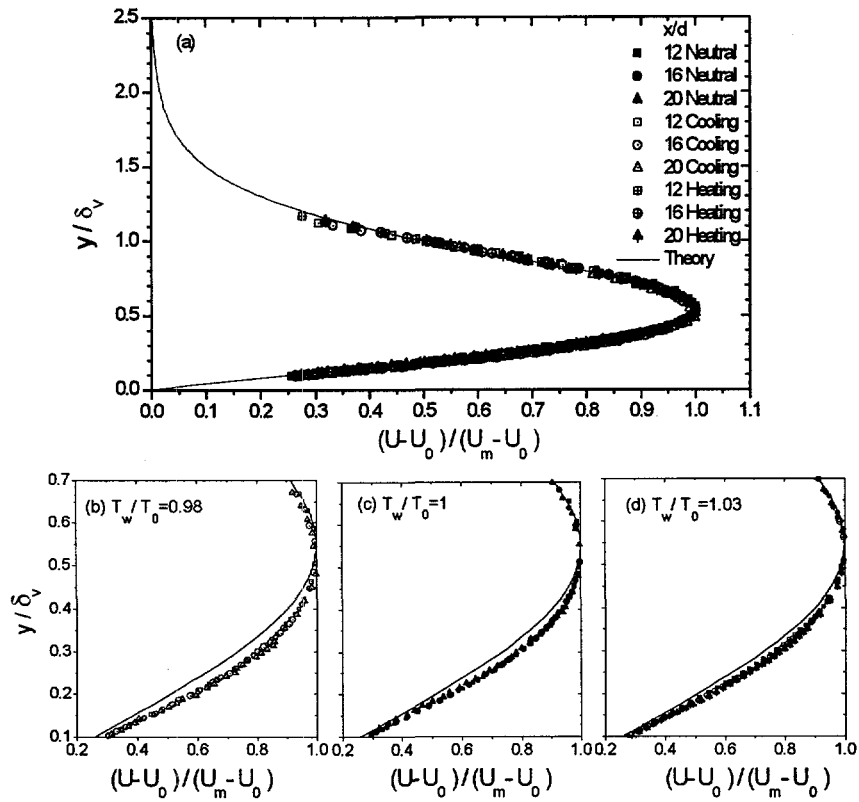
Figure 2: Comparison of normalized velocity profiles at three x/d locations and for $T_w/T_o = 0.98$, 0 and 1.03 (a) full profile, (b), (c) and (d) near-wall region
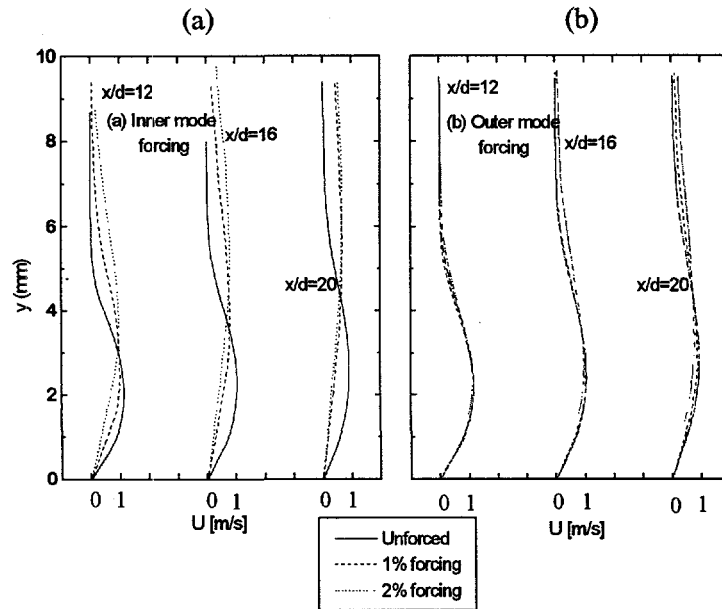

Figure 3: Dimensional mean velocity profiles for various excitation levels and downstream locations (a) inner mode forcing and (b) outer mode forcing for $T_w/T_o = 1.03$.
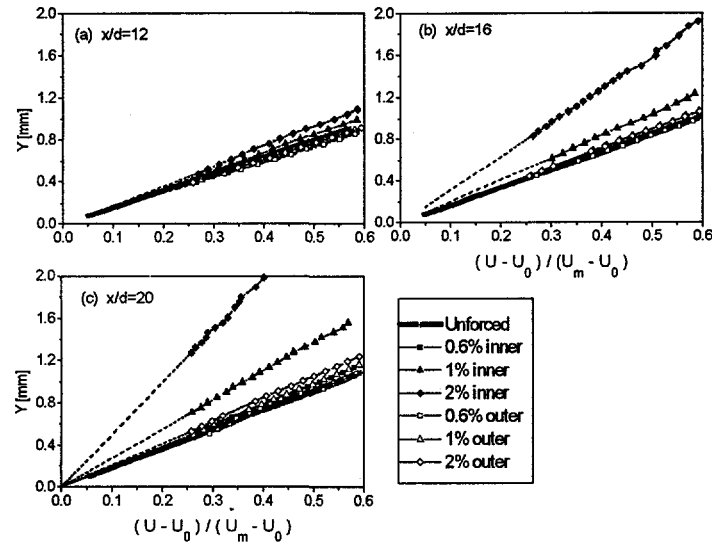
Figure 4: Near-wall velocity gradient comparison for different excitation levels and frequencies at x/d of (a) 12, (b) 16 and (c) 20 and for $T_w/T_o = 1.03$.

The normalized mean temperature profiles measured for the heating case and at $x/d = 16$ are shown in Fig 5a and 5b for inner and outer mode forcing, respectively. As was observed for the velocity field, for low excitation levels the effect of forcing on the temperature profile is negligible. As the excitation level is increased, surprisingly, the temperature gradient near the wall *increases* until an inflection point is formed on the temperature profile. Again, the effect of the inner mode forcing is much more significant. The effect of forcing on the near-wall region of the temperature profile is presented in Fig 6. Low excitation levels do not alter the temperature gradient near the wall, while increasing the excitation level causes an increase in the temperature gradient. Outer and inner mode forcing at 2% excitation level increases the temperature gradients by up to 20% and 45%, respectively. The augmentation in the heat transfer is accompanied by a net reduction in the time-averaged wall drag, a result which could not be anticipated.
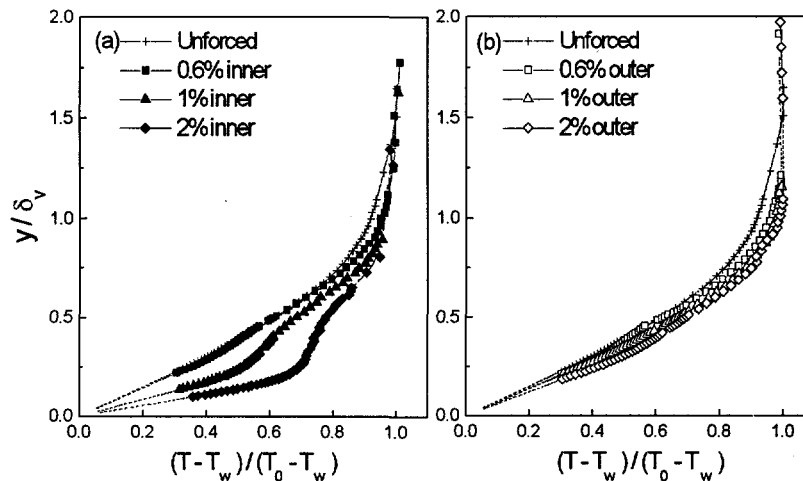

Figure 5: Comparison of normalized temperature profiles measured at $x/d = 20$ and for different excitation levels for (a) inner mode forcing and (b) outer mode forcing for $T_w/T_o = 1.03$.
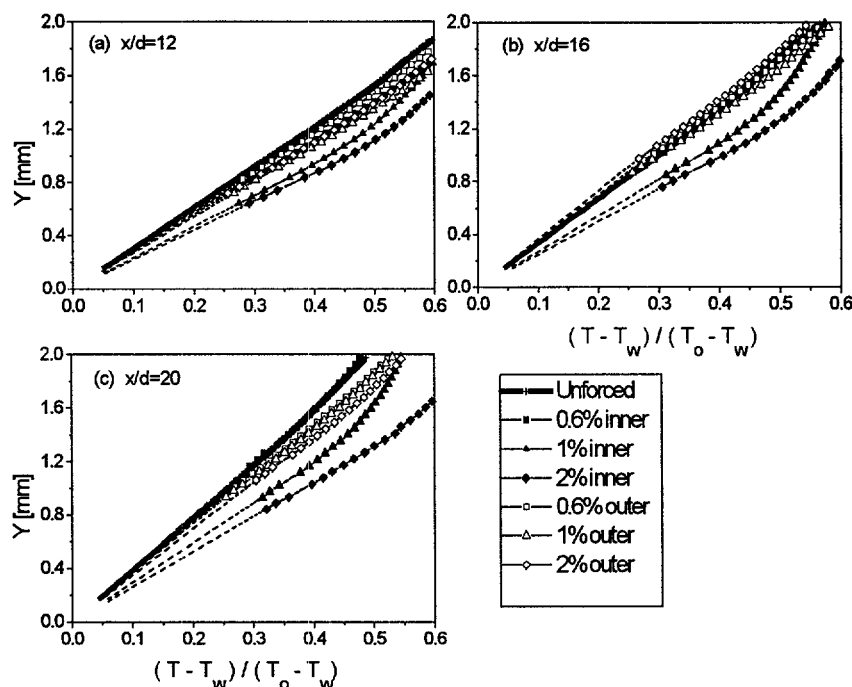
Figure 6: Near-wall temperature gradient comparison for different excitation levels and frequencies at x/d of (a) 12, (b) 16 and (c) 20 and for $T_w/T_o = 1.03$.

As shown in Fig 5 high levels of forcing introduce non-linear effects as observed by a dramatic thickening of the boundary layer. Large scales associated with the outer region become more significant. As was shown by Bajura & Catalano (1975) and Amitay & Cohen (1996) two rows of counter rotating vortices associated with the two regions of the wall jet are present in laminar to turbulent transition. It is the outer row of vortices (which rotate in the counter-clockwise direction and thus transport momentum away from the wall) that receive most of the energy under high levels of forcing and therefore, decrease the velocity gradient near the wall. We hypothesize that this same motion is responsible for the increase in the near-wall temperature gradient which was observed in Figs. 5 and 6. It is plausible that the large vortices in the outer region transport fluid away from the wall to the outer region (which is at a different temperature) and also entrain fluid towards the wall. This motion may also explain the large reduction in the temperature gradient, occurring at y/δ_v of about 0.2 as seen in Fig 5, because the unsteady upward advective transport is increased compared to diffusive transport in this region. This enhanced thermal mixing is manifested also in the observed increase in the wall temperature gradient and thus the wall heat flux.

Fluctuating Quantities

Since the evolution of controlled disturbances apparently is a primary factor in augmenting the heat transfer, the structure and evolution of the temperature and streamwise velocity fluctuations were investigated in detail. In order to obtain phase information, phase-locked data were measured and analyzed for low and high levels of excitation corresponding to the two modes of instability associated with the wall jet flow. These levels of excitation correspond to the linear and nonlinear transitional behavior of the flow. Figure 7 shows the dimensional fluctuating temperature distribution versus the dimensional distance from the wall. The data were taken using the conventional phase-locked technique, and were measured at $x/d = 16$ for $T_w/T_o = 1.03$ and for three excitation levels of (a) 0.6%, (b) 1%, and (c) 2%. A single peak is present for 0.6% forcing, as is shown in Fig 7a. This peak is located at the same distance from the wall for

124

both inner and outer mode forcing. The magnitude of this peak for inner mode forcing is higher due to higher initial growth rates associated with this mode. As the level of forcing is increased, a second peak is formed on the distribution very close to the wall. This second peak occurs at the same location as the inflection point in the mean temperature profile, and is most likely due to a maximum in the unsteady normal velocity v' occurring at this location. Also, the width of the disturbed region is much thicker for inner mode forcing due to the increase of the boundary layer thickness. Similar trends occurred when the wall was cooled.

Figure 8 shows the normalized distribution of the fluctuating fundamental streamwise velocity for an excitation level of 0.6% and for both heating (a) and cooling (b) for outer mode forcing. The distribution contains two large peaks corresponding to the velocity gradient near the wall and the inflection point in the outer region, as was explained by Mele et al. (1986). The outer peak is initially larger and has a broader disturbed region than the inner peak because the above mentioned forcing frequency prevails in the outer region. In both cases, as the downstream distance increases, the ratio between the inner and outer peaks is increased which is consistent with linear stability theory. According to the linear stability theory, as the downstream distance is increased smaller scales governed by the near wall region become more dominant. For a fixed downstream location, the ratio between the inner and outer amplitude maxima is larger for the cooling case. In order to further understand the effect of forcing on the velocity field, the effect of the level of excitation was also addressed. In Fig 9, two cases of inner mode forcing corresponding to (a) 0.6% and (b) 2% are presented for three downstream locations. δ_v was used to normalized the normal distance from the wall which is consistent with the stability theory. The inner peak is significantly higher, as expected, because the effect of inner mode forcing is most dominant in the inner region. For the low excitation level of 0.6%, the ratio between the inner to outer maxima increases with the downstream distance as was observed when outer mode forcing was applied in Fig 8. This is once again consistent with linear stability theory. However, for the 2% forcing the trend is the opposite, with the ratio between the inner to outer maxima decreasing with downstream location. This is probably due to the fact that for high excitation levels non-linear mechanisms are introduced. At any given x/d, the boundary layer is much thicker and therefore large scales, corresponding to low frequencies, prevail throughout the flow field. As was mentioned before, when the forcing frequency is low, the outer maxima dominates the fluctuating streamwise velocity distribution since it corresponds to the large scales.
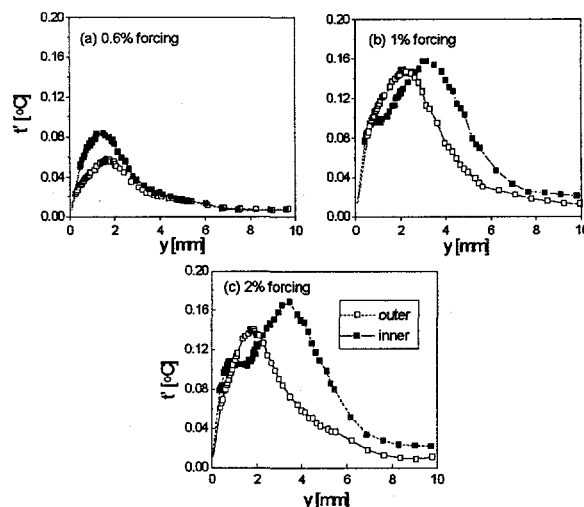

Figure 7: Fluctuating temperature distribution for inner and outer mode forcing for (a) 0.6%, (b) 1% and (c) 2% excitation levels (x/d = 16 and T_w/T_o = 1.03).
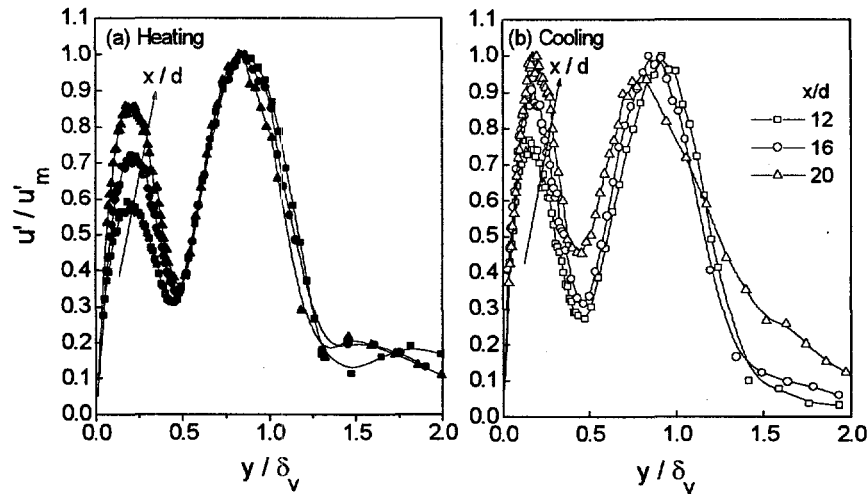
Figure 8: Normalized fluctuating streamwise velocity comparison at three x/d locations and for outer mode forcing at excitation level of 0.6%, (a) wall heating and (b) wall cooling.
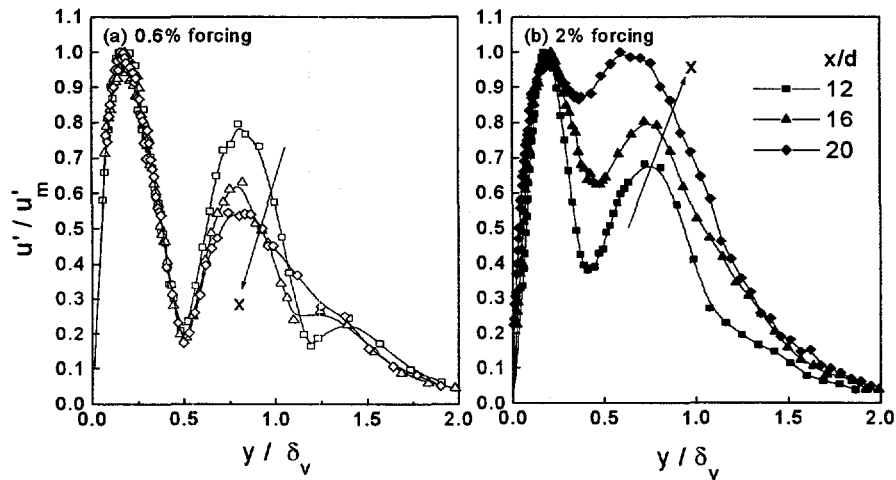

Figure 9: Normalized fluctuating streamwise velocity comparison at three x/d locations and for inner mode forcing, (a) 0.6% and (b) 2% excitation levels and $T_w/T_o = 1.03$.

NUMERICAL SIMULATIONS

Numerical Methods

In parallel to the experimental investigations, Direct Numerical Simulations (DNS) were conducted based on the complete Navier-Stokes equations. For these simulations, two computer codes were employed that were developed for investigating transition in boundary layers, both for compressible and incompressible flows. Both codes, compressible and incompressible, were modified and adapted to the wall jet geometry. In the compressible Navier-Stokes code, the complete Navier-Stokes equations, the energy equation, and the continuity equation are solved in conservative formulation. The fluid is modeled as a calorically perfect gas and Sutherlands Law is used to calculate the viscosity from the temperature. The

time integration was performed using a 4th-order Runge-Kutta method. For the spatial discretization a 4th order upwind-downwind "splitting" scheme was used. For the results shown here, an equidistant grid in the x- and y-direction was used. In the spanwise direction, a pseudo-spectral approach was chosen. In the incompressible Navier-Stokes code the Navier-Stokes equations are solved in the vorticity-velocity formulation in conjunction with the energy equation. A fourth-order polynomial is used for the temperature dependence of viscosity and thermal conductivity. As for the compressible code, time integration is performed using a 4th-order Runge-Kutta method. The streamwise and wall normal directions are discretized using 4th-order split differences. The solution procedure of the viscous terms in the vorticity transport equations was extensively modified to facilitate the introduction of a subgrid-scale (SGS) turbulence model to be used for Large-Eddy-Simulations. A equidistant grid is used in the streamwise direction, whereas in the wall normal direction, a stretched grid is used where points are clustered near the wall.

Computational Results

Before applying the codes to extensive simulations of our laboratory experiments, the codes were extensively tested and validated to demonstrate their ability and efficiency of obtaining results. In both the compressible and incompressible simulations, disturbances are introduced into the flow field by periodic blowing and suction through a slot in the wall near the inflow boundary (see Fig. 10). For this forcing, the stream wise distribution of the disturbance velocity is such ,that the net mass flux is zero. Therefore, predominantly vorticity disturbances of a specified frequency are introduced. Using these two entirely different numerical approaches, we can validate our calculations by comparing the results of the compressible and incompressible simulations, even in flow regimes that are outside the scope of Linear Stability Theory and our experiments. Both codes (compressible and incompressible) were extensively tested by comparison calculations with linear stability theory. These calculations showed that the codes are efficient and reliable. For calculating the base flow, the similarity solution for the appropriate nondimensional temperature difference between wall and ambient is used as initial condition. Using pseudo-time stepping, the calculation is continued until a given convergence criterion is satisfied. Using these base flows, numerous unsteady simulations were performed for an isothermal, cooled and heated wall jet. With the compressible code, all calculations were done for a global Mach number of M=0.3, based on the maximum velocity at the inflow and the speed of sound in the ambient fluid. This Mach number allows for reasonably large time steps and ensures that compressibility effects are still negligible. A comparison of the amplitude and phase development over the streamwise coordinate x is shown in Fig. 11. The agreement of the compressible and incompressible simulations is excellent.
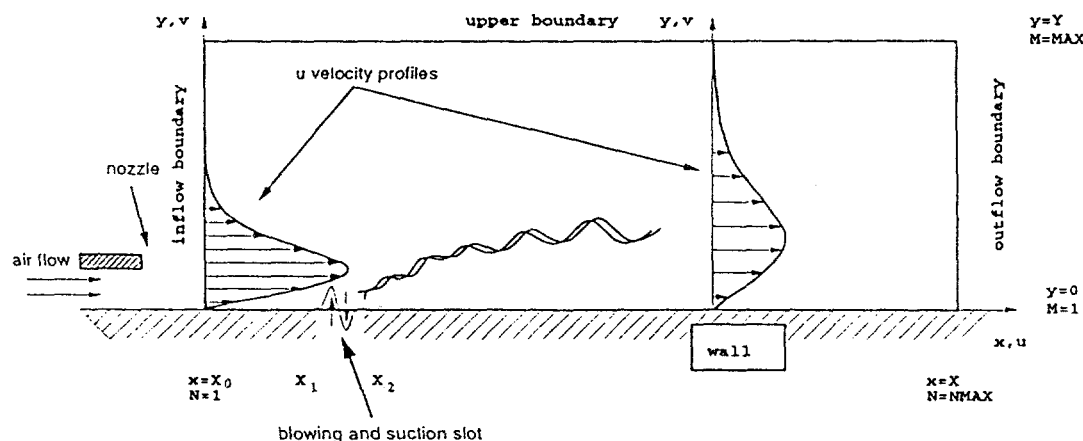

Figure 10. Computational domain for numerical simulations.

In Fig. 11, there is a slight deviation of the numerical results compared to the results obtained from Linear Stability Theory. This difference is due to the fact that Linear Stability Theory can only take local effects into account, whereas our simulations follow the development of the disturbances downstream of the blowing and suction slot. In this particular case, the slot was located upstream of the unstable region of the shear layer mode (outer mode), so that this mode was amplified first. Although it is damped in the region shown, it still has a finite amplitude and it takes some downstream distance until its influence on the velocity maximum is negligible compared to the boundary layer mode. From this point on, the agreement of the results from the numerical simulations and Linear Stability Theory is excellent. Figure 12 shows the eigenfunctions of the streamwise- and wall normal velocity, u and v. Again, the results of the compressible and incompressible simulations show excellent agreement. These results indicate that with our calculations, we are able to capture the relevant physical mechanisms in the flow. Furthermore, we are convinced that the codes are usable for simulations of highly nonlinear flow configurations. For a detailed comparison with the ongoing laboratory experiments, a new set of simulations was started for the case with weak wall heating, using the incompressible code. To account for the effect of the unheated starting length that was found in the experiments, the concept of the artificial Prandtl number (discussed in an earlier report) was utilized and we were able to obtain very good agreement of the experimental and computational mean flow profiles. The linear stability diagram for the case with a heated wall (T_w=32.5 C, T_0=24 C, F=43.5Hz) is shown in Fig. 13. The solid line indicates the Reynolds number/wave number pairs at which the experiments were conducted. Using small amplitude disturbances, the results of experiments and calculations can be compared with Linear Stability Theory. The baseflow u velocity and temperature profiles, as well as the eigenfunctions u' and t', at x/d=20 are shown in Fig. 14. The calculations are in very good agreement with the experiments.
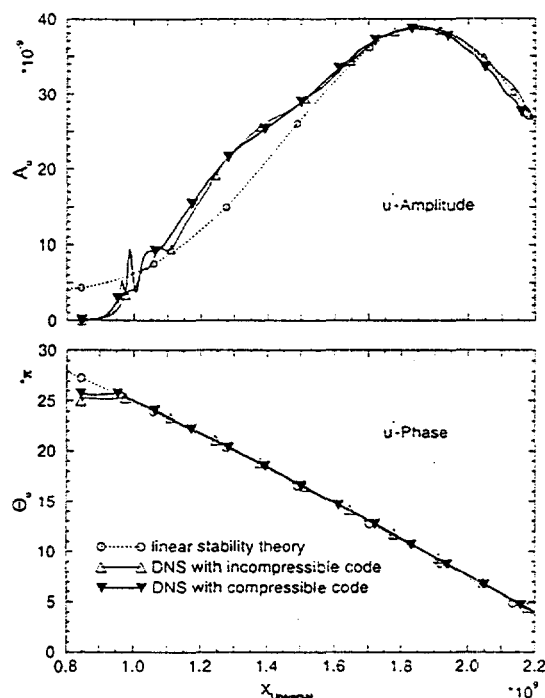

Figure 11. Downstream development of u'-amplitude and phase u'. Comparison of results obtained from compressible and incompressible code with linear stability theory.
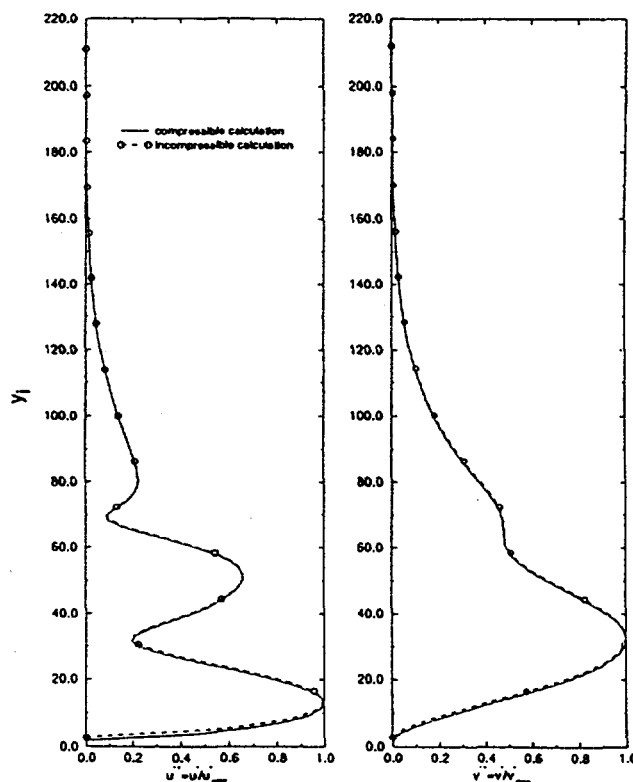
Figure 12. Comparison of amplitude distributions (eigenfunctions) obtained for compressible and incompressible code (a) u'-amplitude, (b) v' amplitude

Using larger forcing amplitudes, large changes in the mean flow profiles due to nonlinear effects can be observed (see Figs. 3 and 5). The shear stress at the wall is reduced and the heat transfer from the wall is increased, in qualitative agreement with the experiments. A quantitative comparison is very difficult because of the high turbulence level (0.5%) in the experimental facility. This "noise" introduces energy into the flow that cannot easily be taken into account in the numerical simulations. For investigations of turbulent wall jets, codes for compressible and incompressible Large Eddy Simulations (LES) are being developed. The incompressible code is currently being used for the calculation of transitional and turbulent flat plate boundary layers with zero and strong adverse pressure gradients. We are confident that the turbulence model used in these simulations can be adapted with only minor modifications for the investigations of turbulent wall jets.
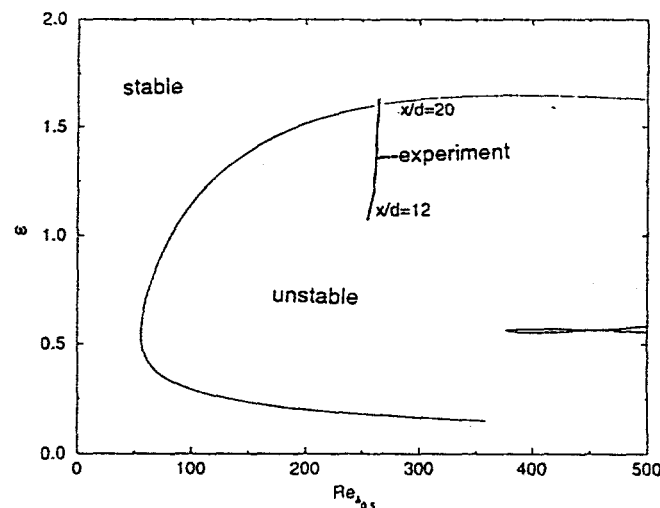

Figure 13. Stability diagram of linear stability theory for wall jet with wall temperature T_w; solid line corresponds to downstream domain of experiments.
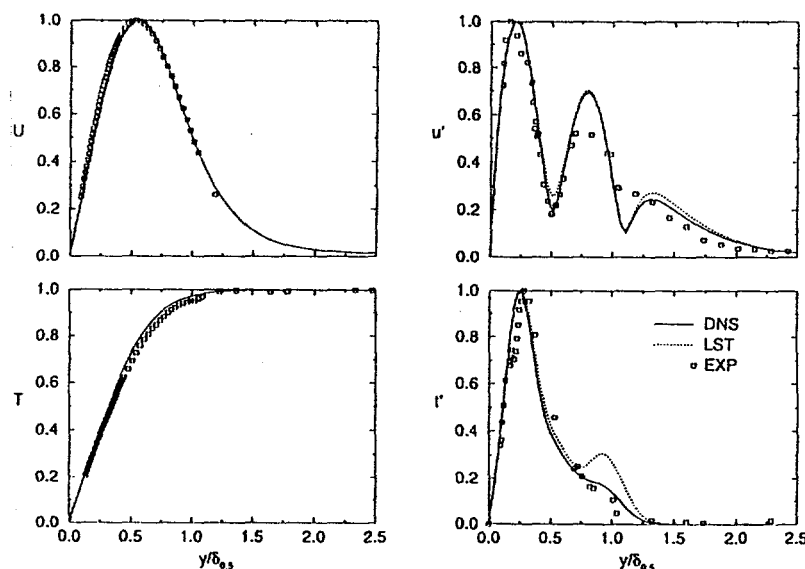

Figure 14. Comparison of experimental measurements, linear stability theory, and Direct Numerical Simulations for Tw=32.5 C, To=24 C, F=43.5 Hz, x/d=20. (a) u-velocity, (b) temperature, (c) amplitude distributions (eigenfunction) for u' fluctuations, (d) amplitude distributions for t' fluctuations.

129

CONCLUSIONS

In order to better understand the heat and momentum transfer associated with complex unsteady film-cooling problems, the plane, laminar, wall jet was investigated experimentally, theoretically, and numerically for the constant wall temperature boundary condition and with no freestream flow. Measured streamwise mean flow velocity profiles for the unforced case for small temperature differences (6-8 C) were compared to the theoretical predictions. When cooling was applied, the inner velocity gradient was the highest and the maximum velocity was shifted closer to the surface, while heating the surface had the opposite effects. Disturbances were introduced at excitation levels of 0.6%, 1% and 2% and at two forcing frequencies corresponding to the inner and outer modes associated with the wall jet. High levels of forcing (1% and 2%) greatly altered the velocity and temperature profiles. The most significant effects occurred for inner mode forcing where the total skin friction drag (integrated effect) was *reduced* by 45% and the total heat flux was *increased* by 20%. The skin friction and wall heat flux were less susceptible to outer mode excitation but the trends were not altered. The same results occurred for both heating and cooling of the surface. Inner mode forcing had the most significant effects on the velocity and temperature fields. The initial spatial growth rates associated with the inner mode are greater than the outer mode growth rates. We hypothesize that it is the outer row of counter-rotating vortices that receive most of the energy under high levels of forcing and therefore, *decrease* the velocity gradient near the wall. These large vortices enhance thermal mixing and produce the observed *increase* in the temperature gradient near the wall.

ACKNOWLEDGMENTS

REFERENCES

1. Amitay, M. and Cohen, J., 1993, "The Mean Flow of a Laminar Wall Jet Subjected to Blowing or Suction", *Phys. Fluids*, A 5, 2053.
2. Amitay, M. and Cohen, J., 1996, "Transition in a Two-Dimensional Plane Wall Jet Subjected to Blowing or Suction", submitted to *J.Fluid Mech.*
3. Bajura, R. A. and Catalano, M. R., 1975, "Transition in a Two-Dimensional Plane Wall Jet", *J. Fluid Mech.*, Vol. 70, part 4, 773-799.
4. Bajura, R. A. and Szewezyk, A., 1970, "Experimental Investigation of a Laminar Two-Dimensional Plane Wall Jet", *Phys. Fluids*, 13, 1653.
5. Chun, D. H. and Schwarz, W. H., 1967, "Stability of the Plane Incompressible Viscous Wall Jet Subjected to Small Disturbances", *Phys. Fluids*, 10, 5, 911-915.
6. Cohen J., Amitay M. and Bayly, B.J., 1992, "Laminar-Turbulent Transition of Wall Jet Flows Subjected to Blowing and Suction", *Phys. Fluids* A 4, 283.
7. Glauert, M.B., 1956, "The Wall Jet", *J.Fluid Mech*, 1, 625-643.
8. Katz, Y., Horev, E. and Wygnanski, I., 1992, "The Forced Turbulent Wall Jet", *J.Fluid Mech*, 242, 577-609.
9. Kline, S. J., and McClintock, F. A., 1953, "Describing Uncertainties in Single Sample Experiments," *Mechanical Engineering*, Vol. 75, Jan., pp. 3-8.
10. Mele, P., Morganti, M., Scibillia, M. F. and Lasek, A., 1986, "Behavior of Wall Jet in Laminar-to-Turbulent Transition", *AIAA Journal*, 24, 938-939.

11. Mitachi, K & Ishiguro, R., 1974, "Heat Transfer of Wall Jets", *Heat Transfer: Japanese Research*, 27-40.
12. Riley, N., 1958, "Effects of Compressibility on a Laminar Wall Jet", *Jornal of Fluid Mechanics*, **4**, 615-628.
13. Tetervin, N., 1948, "Laminar Flow of a Slightly Viscous Incompressible Fluid that Issues from a Slit and Passes over a Flat Plate", NACA TN, No. 1644.
14. Schwarz W. H. and Caswell B., 1961, "Some Heat Transfer Characteristic of the Two-Dimensional Laminar Incompressible Wall Jet", *Chemical Engineering Science*, **16**, 338-351.
15. Schwarz W. H. and Caswell B., 1961, "Some Heat Transfer Characteristic of the Two-Dimensional Laminar Incompressible Wall Jet", *Chemical Engineering Science*, **16**, 338-351.
16. Zhou, M. D., Heine, C. and Wygnanski, I., 1993, "The Forced Wall Jet in an External Stream", *AIAA* 93-3250.